2007

A Study Of Equatorial Ionopsheric Variability Using Signal Processing Techniques

Xiaoni Wang
University of Central Florida

A STUDY OF EQUATORIAL IONOSPHERIC VARIABILITY USING SIGNAL PROCESSING TECHNIQUES

by

XIAONI WANG
M.S. University of Central Florida, 2004

A dissertation submitted in partial fulfillment of the requirement
for the degree of Doctor of Philosophy
in the Department of Electrical and Computer Engineering
in the School of Electrical Engineering and Computer Science
at the University of Central Florida
Orlando, Florida

Spring Term
2007

Major Professor: Richard Eastes

ABSTRACT

The dependence of equatorial ionosphere on solar irradiances and geomagnetic activity are studied in this dissertation using signal processing techniques. The statistical time series, digital signal processing and wavelet methods are applied to study the ionospheric variations. The ionospheric data used are the Total Electron Content (TEC) and the critical frequency of the F2 layer (foF2). Solar irradiance data are from recent satellites, the Student Nitric Oxide Explorer (SNOE) satellite and the Thermosphere Ionosphere Mesosphere Energetics Dynamics (TIMED) satellite. The Disturbance Storm-Time (Dst) index is used as a proxy of geomagnetic activity in the equatorial region. The results are summarized as follows. (1) In the short-term variations $\leq$27-days, the previous three days solar irradiances have significant correlation with the present day ionospheric data using TEC, which may contribute 18% of the total variations in the TEC. The 3-day delay between solar irradiances and TEC suggests the effects of neutral densities on the ionosphere. The correlations between solar irradiances and TEC are significantly higher than those using the F10.7 flux, a conventional proxy for short wavelength band of solar irradiances. (2) For variations $\leq$ 27 days, solar soft X-rays show similar or higher correlations with the ionosphere electron densities than the Extreme Ultraviolet (EUV). The correlations between solar irradiances and foF2 decrease from morning (0.5) to the afternoon (0.1). (3) Geomagnetic activity plays an important role in the ionosphere in short-term variations $\leq$10 days. The average correlation between TEC and Dst is 0.4 at 2-3, 3-5, 5-9 and 9-11 day scales, which is higher than those between foF2 and Dst. The correlations between TEC and Dst

increase from morning to afternoon. The moderate/quiet geomagnetic activity plays a distinct role in these short-term variations of the ionosphere (~0.3 correlation).

For my parents

and Michael

ACKNOWLEDGMENTS

I would like to thank Dr. Tom Woods for providing the solar irradiances from the TIMED satellite.

I thank Dr. Scott Bailey for providing solar irradiance data from the SNOE satellite.

I am grateful for Dr. Cesar Valladares who provided the TEC data and instructed to properly use the data.

I am thankful for Dr. Bodo Reinisch for providing the foF2 data.

I thank Dr. Stephen Weichecki Vergara for his efforts and suggestions in the time series analysis.

I am thankful for Dr. Sun's precious advice and help in wavelet methods.

I thank Dr. Linwood Jones, Dr. Stephen Waston and Dr. Sen Shivamoggi for being the dissertation committee member.

I am deeply in debt to Dr. Richard Eastes. As my advisor, he has graciously supported, advised and encouraged me in my research. He has showed me the wonderful picture of space physics which I would like to explore more. I have been amazed by his broad knowledge, the depth of his understandings and eagerness to learn more. I also owe him a lot for his efforts to improve my English writing.

TABLE OF CONTENTS

LIST OF FIGURES

LIST OF TABLES

CHAPTER ONE
INTRODUCTION

1.1 Background

The solar-terrestrial environment includes solar emissions, the geomagnetic field and the Earth's atmosphere. Earth's atmosphere extends to distances measured in tens of earth radii. The upper atmosphere, above 100km, absorbs most of the energetic solar radiation, *i.e.*, extreme ultraviolet (EUV) and X-ray radiation. This radiation penetrates and ionizes the upper atmosphere, producing significant numbers of free electrons and ions. The ionized part of the atmosphere is called the *ionosphere.* Shown in Figure 1 is the typical vertical structure of the ionosphere. The main regions are designated as D, E and F, with the F region having the highest electron density.

Several factors affect ionospheric electron densities. Besides the solar EUV and X-ray radiation, geomagnetic disturbances within the magnetosphere have a significant effect. The magnetosphere, a domain where the Earth's magnetic field dominates, consists of thermal plasma and energetic charged particles of both the solar wind and terrestrial origin. The strength and form of the magnetospheric effects are primarily determined by the solar wind dynamic pressure and the orientation of the interplanetary magnetic field (IMF, *i.e.*, the state of the interplanetary medium). Also, tides and gravity waves propagate up to the mesosphere (which extends from 50-85 km) and directly affect the neutral densities which in turn affect the

ionospheric densities. Due to the coupling with other regions, understanding ionospheric variability is a challenge.

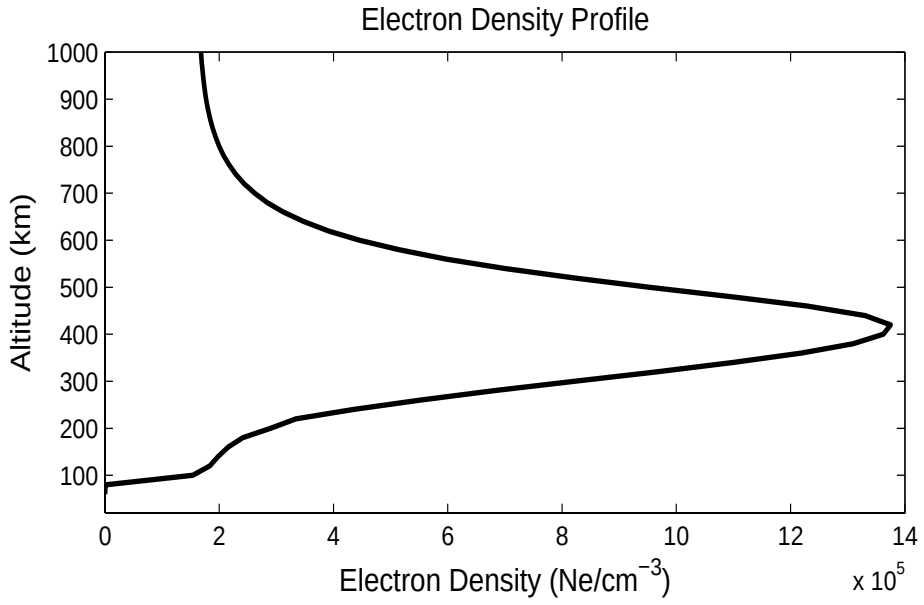

Figure 1. Typical vertical profile of electron density

1.2 The Challenges

The lack of direct solar irradiance measurements presents a challenge in the study of the solar-terrestrial environment. It is well understood that solar EUV produces the F region, and unraveling the interaction between the densities and solar irradiance would improve capabilities for forecasting the ionosphere. Most studies have used proxies, like the F10.7 radio flux, as a substitute for solar EUV when studying the effects of solar irradiances on the ionosphere [*e.g.*, *Forbes et al.,* 2000; *Liu et al.,* 2000], but the expected linear relationship between ionospheric

densities and F10.7 breaks down for high values of F10.7 [*Kane*, 1992; *Rishbeth*, 1993; *Balan et al.*, 1994]. Therefore, proxy based studies of ionospheric densities and solar variations are not completely reliable, and an examination using short wavelength solar irradiances is needed to improve our understanding of their relationship.

Geomagnetic disturbances were found to be accompanied by large changes in the F2-layer by *Appleton and Ingram* [1935]. Most recent work on geomagnetic disturbances has concentrated on storm times. Such disturbances may disrupt radio communications and cause power blackouts. A comprehensive study of the ionosphere's response to magnetic storms is currently being conducted by scientists under a program sponsored by the National Science Foundation (NSF), known as Coupling Energetics and Dynamics of Atmospheric Regions (CEDAR). An initial study was conducted for storms that occurred in September 1984, a period of low solar activity. The second study chose March 16-23, 1990, a period near solar maximum. Furthermore, the effects of electric fields and neutral winds on the low-middle latitude ionosphere have been discussed [*Richards et al.,* 1993, *Buonsanto et al.,* 1993]. Recent studies on the storm-time ionosphere have expanded to neutral densities and more layers of atmosphere [*e.g.*, *Rishbeth,* 1991; *Field and Rishbeth,* 1997; *Basu et al.,* 2001; *Daniell and Strickland,* 2001; *Strickland et al.* 2001a, 2001b; *Fuller-Rowell et al.,* 2002].

While these storm-time studies have improved our understanding of how the space environment responds when the energy deposited changes dramatically, the space environment is a non-stationary system. In order to fully understand how the ionosphere varies in response to events of different magnitudes, studies based on a wide range of conditions and over extensive time spans are needed. Since smaller events are significantly more numerous, the statistical

uncertainty in determining relationships between inputs and responses in the space environment may be less than one obtains when studying the largest events. However, successfully dealing with the larger quantities of data available for the smaller events is a challenge that has usually been avoided.

1.3 Goal of the Dissertation

Recent measurements of the short wavelength solar irradiance provide an opportunity to improve our understanding of their correspondence with ionospheric densities. Photometers on the Student Nitric Oxide Explorer (SNOE) satellite began daily measurements of the solar soft X-ray irradiances (0.1 nm-20 nm) from March 1998 [*Bailey et al*., 2000 and 2005]. The Solar Extreme-ultraviolet Experiment (SEE) aboard the Thermosphere Ionosphere Mesosphere Energetics Dynamics (TIMED) spacecraft has measured the solar spectral irradiance (0-193 nm) in the X-ray ultraviolet (XUV), extreme ultraviolet (EUV), and far ultraviolet (FUV) ranges since February 2002 [*Woods et. al.,* 1998, 1999a, 2005]. These direct measurements of the Sun's short wavelength emissions should enable us to better understand the effect of solar irradiances on the ionosphere.

Besides these newly available solar data, geomagnetic indices have been used to measure geomagnetic activity for decades. There are several popular indices such as Kp, ap and Dst, and a complete description of these indices has been given by *Mayaud* [1980]. The Dst index is derived from magnetometer measurements near the equator and it is a measure of the geomagnetic activity at low latitudes. Compared to Kp and ap, which measure geomagnetic

activity in the auroral and subauroral areas, the Dst index is more representative of equatorial geomagnetic activity.

Measurements of the ionosphere have been made by various techniques, first with bottom side ionosondes, and then by incoherent scatter radars. Topside sounders on satellites were later used, followed by GPS networks and receivers. The critical frequency of the F2 layer (foF2), measured by ionosondes (and digisondes), has been widely used for years [*e.g., Rishbeth,* 1991; *Fuller-Rowell et al.,* 1994; *Field and Rishbeth*, 1997; *Forbes et al.,* 2000; *Mendillo et al.,* 2001]. GPS receivers can provide the Total Electron Content (TEC) along a line of sight through the ionosphere [*Pi et al.*, 1997; *Kelly et al.,* 1996; *Lunt et al.,* 1999 a and b; *Kutiev et al.,* 2005; *Valladares et al.,* 2001].

The goal of this dissertation is to use the above-mentioned data to study the dependence of ionosphere on solar irradiance and geomagnetic activity. The TEC data are from a GPS receiver in Ancon, Peru and the foF2 are from a digisonde at the Jicamarca Radio observatory in Peru. These ionospheric data are compared with solar irradiance data from the SNOE and TIMED satellites, as well as Dst data from equatorial magnetometers. The examination begins from a stationary perspective, in both the time and frequency domains, by utilizing techniques such as time series analysis and digital signal processing (Chapter 3 and 4), and then from a non-stationary perspective by using wavelet methods (Chapter 5). The dissertation is organized in the following way: (1) Chapter 2 introduces the background of the signal processing techniques and instruments used; (2) Chapter 3 examines the relationship between TEC and solar irradiances; (3) Chapter 4 discusses foF2 and solar irradiances; (4) Chapter 5 studies geomagnetic activity and ionosphere; (5) Chapter 6 presents a summary of this dissertation and future work.

CHAPTER TWO
SIGNAL PROCESSING TECHNIQUES AND INSTRUMENTS

This chapter introduces the signal processing techniques and the instruments used to collect the data analyzed in this dissertation.

2.1 Signal Processing Techniques

2.1.1 Introduction

A signal is defined as a physical quantity that varies with time, space, or any other variables. A signal varying with time can be continuous or discrete, deterministic or random. A discrete time signal is defined only at specific times; a deterministic signal can be uniquely described by an explicit mathematical expression. In space physics, many signals have deterministic behavior and are measured at specific times for which a relationship is sought.

The relationship between two or more signals can be modeled as a system with inputs and outputs. A system is time invariant if the input-output characteristics do not change with time; otherwise it is time varying. A system is linear if the output is linearly dependent on the input; otherwise it is nonlinear. A linear time-invariant (LTI) system is often assumed in classical signal processing techniques.

Two basic methods have been developed for the analysis of LTI system. One method is based on the direct solution of the input-output equation for the system, which has the form

$$y(n) = F[y(n-1), y(n-2), ..., y(n-N), x(n), x(n-)..., x(n-M)] \quad (2.1)$$

This method, which is used to study systems in the time domain, is sometimes called time series analysis. The second method, which is commonly used to study systems in the frequency domain, decomposes the input signal into a sum of elementary signals based on the Fourier transform. Spectral analysis and digital filter design are two important applications of the second method. Both time series analysis and frequency domain analysis are used in this dissertation to model and transform the signals (Chapter 3 and 4).

The LTI-based signal processing methods may not adequately describe the details of a system in both the frequency and time domain. Several alternate methods have been developed and wavelet methods are used in this dissertation. By decomposing a signal into components with different frequency resolutions, wavelet methods have the advantage of representing short-term variations accurately at both the time and frequency domain. A preliminary study using wavelet methods is presented in Chapter 5.

This section presents the basics of the signal processing techniques used in the dissertation: (1) the introduction of time series analysis; (2) digital signal processing with applications in power spectral estimation and digital filters; (3) wavelet methods and filter banks. A detailed discussion of each topic is presented in the section below.

2.1.2 Time Series Theory

A time series is a set of observations which were recorded at specific times. Good discussions of time series analysis can be found in *Box and Jenkins* [1976], *Anderson* [1971],

Aoki [1987], *Rosenblatt* [1985], *Mendenhall et al* [1990], *Brockwell and Davis* [1991 and 1996], *Bloomfield,* [2000]. This section introduces the basic definitions and analysis procedures of time series analysis. The main purpose of using this method is to find the time-dependent relationships between the signals by properly transforming the data.

2.1.2.1 Basic definitions

Stationary series are commonly the study objects of time series analysis. A series X_t is (weakly) stationary if

(1) The *mean function* $\mu(t)$ is independent of t

$$\mu(t) = E(X_t), \tag{2.2}$$

where X_t is a time series with $E(X_t^2) < \infty$, and $E(X_t)$ is the expectation value of X_t.

(2) The *covariance function* $\gamma(t+h,t)$ is independent of t for each time lag h

$$\gamma(t+h,t) = COV(X_r - X_s) = E[(X_r - \mu(r))(X_s - \mu(s))] \tag{2.3}$$

for all integer r and s. The requirements (2.2) and (2.3) define a second-order stationary series using its mean and its covariance function. Such definition is used in the time series analysis performed in this dissertation (Chapter 3). Transformations are applied for those series which are not stationary.

The covariance function of a second-order stationary series is called the auto-covariance function (ACVF) and denoted as $\gamma(h)$. The *autocorrelation function* (ACF), derived from the ACVF (Equation 2.5), is often used in time series analysis.

ACVF: $\gamma(h) = COV(X_{t+h}, X_t)$ (2.4)

ACF: $\rho(h) \equiv \frac{\gamma(h)}{\gamma(0)} = COR(X_{t+h}, X_t)$ (2.5)

2.1.2.2 Time Series Analysis Procedures

The time series analysis approach used in this dissertation is: (1) plot the series and examine whether there is a trend or a periodic component; (2) remove the trends and periodic components to transform the signal into a stationary one; (3) fit a model to the stationary data; (4) apply statistical tests to the residuals. Procedures (2), (3) and (4) are discussed below.

Trends and periodic variations are often seen in time series. A trend represents a linear or (most often) nonlinear component that changes over time and does not repeat within the time range of the data used, while a periodic variation repeat itself over time. Both components can be seen in real signals.

There are various ways to remove trends and periodic variations. A moving average is often used to estimate a trend and then removed from the signal. Letting q be a nonnegative integer, a two-sided moving average for a time series X_t is defined as

$$W_t = (2q+1)^{-1} \sum_{j=-q}^{q} X_{t-j} \quad (2.6)$$

Differencing is an effective approach to remove periodic variations from a signal [*Box and Jekins*, 1976]. A periodicity of period d can be removed by using the lag-d differencing operator ∇_d defined by

$$\nabla_d X_t = X_t - X_{t-d} \tag{2.7}$$

The moving average and differencing methods are used in Chapter 3 and 4 to remove the trends and periodic variations in the data.

After the trends and periodic variations are removed, a linear mathematical model can then be applied to fit the stationary time series. The Autoregressive (AR) models, Moving Average (MA) models and Autoregressive-Moving Average (ARMA) models are used in this dissertation. A detailed description of these models and algorithms can be found in *Brockwell and Davis* [1996].

An AR model is a linear regression of the current value of a series against one or more previous values of the series, as is defined in Equation (2.8). The value of p is called the order of the AR model. A MA model represents the current values of a signal by using a linear combination of the current and previous values of a random signal, as defined in Equation (2.9). The value of q is called the order of the MA model. An ARMA model incorporates an AR and MA model as displayed in Equation (2.10).

$$X_t - \phi_1 X_{t-1} - ...\phi_p \; X_{t-p} = Z_t \tag{2.8}$$

$$X_t = Z_t + \theta_1 \; Z_{t-1} + ...\theta_q \; Z_{t-q}, \tag{2.9}$$

$$X_t - \phi_1 \; X_{t-1} - ...\phi_p X_{t-p} = Z_t + \theta_1 \; Z_{t-1} + ...\theta_q \; Z_{t-q}, \tag{2.10}$$

where $Z_t \sim \; WN(0, \sigma^2)$ and $t = 0, \; 1, ...N$. These models are used in Chapter 3, where the details of their application can be found.

Lastly, statistical tests are introduced which are used to evaluate the characteristics of the data. For a series with a large data size n and a finite variance, if 95% of the sample ACF falls between the bounds $\pm \frac{1.96}{\sqrt{n}}$, the series is an IID series; otherwise, mathematical models are needed to fit the series.

2.1.2.3 Multivariate Time Series analysis

In the previous section we discussed the analysis of one stationary series, called *univariate time series analysis*. In order to study the relationships between multiple variables, *multivariate time series analysis* is needed. A detailed description of multivariate analysis can be found in *Brockwell and Davis* [1996]. Much of the theory of univariate time series can be naturally extended to the multivariate case. The univariate analysis approach is used in this dissertation to transform individual signals prior to studying their interdependent relationships.

In order to study the relationships between multiple stationary series, the *cross-correlation function* (CCF) is calculated. For two stationary signals X_t and Y_t, the CCF is defined as

$$\gamma_{xy}(t+h,t) = E[(X_r - \mu_x(r))(y_s - \mu_y(s))] \tag{2.11}$$

where $h = 0,\pm1,\pm2...$ The CCF represents the correlations between X_t and Y_t at different time lag h. According to Theorem 2.1 (seen in Appendix A), the autocorrelations of each series can affect the cross-correlations between the series. In order to obtain an accurate representation of the relationships, removing the autocorrelations is an essential step. Such a step, by fitting a

proper mathematical model to individual series, can transform the series into white noise. This procedure is sometimes called *prewhitening.* The whiteness of the modeling residuals are examined using the statistical IID test.

2.1.2.4 Summary

As a summary, time series analysis uses the mean, autocovariance function and cross-correlation function to give a clear time-dependent picture for a system. It is widely used in modeling and forecasting in the economic, scientific and engineering fields. Other signal analysis methods which are commonly based on frequency domain analysis are presented below.

2.1.3 Digital Signal Processing

Digital signal processing began with the development of algorithms for the fast calculation of the discrete Fourier transform. Digital signal processing has two important applications: spectral analysis which is used to study the power spectrum of the signals and digital filters which are used to represent variations in the frequency domain.

2.1.3.1 Spectral analysis

Various methods for spectral analysis can be categorized as non-parametric, parametric and subspace methods. Good discussions about spectral analysis are seen in *Oppenheim et al.,*

[1989], *Duhamel et al.,* [1990] and *Proakis et al.,* [1996]. These methods are used to analyze the data in Chapter 3 and 4.

The nonparametric methods are commonly based on the Fourier transform. For a discrete signal $x(n)$ with a size of N, the Fourier transform decomposes a signal into a sum of sinusoids of different frequencies, as shown in Equation 2.12. The power spectrum of the signal can be obtained by a direct modification of the Fourier transform, which is called the periodogram method, as shown in Equation 2.13.

$$X(k) = \frac{1}{N}\sum_{n=0}^{N-1} x(n)e^{-j2\pi kn/N} \qquad 0 \le k \le N-1 \tag{2.12}$$

$$P\left(\frac{K}{N}\right) = \frac{1}{N}\left|\sum_{n=0}^{N-1} x_i e^{-j2\pi kn/N}\right|^2 \qquad 0 \le k \le N-1 \tag{2.13}$$

Other methods, such as the Bartlett method, Welch's method, and the Black-Tukey method, make further modifications to the periodogram to reduce the variance of the power spectrum estimation. Welch's method [*Welch*, 1967], which is used in Chapter 3 and 4, has good estimation quality and can be conveniently used for study since it has been programmed into MATLAB. Welch's method includes several steps of modifications. First, the signal is subdivided into segments which allow overlaps. Second, the data in each segment are windowed prior to computing the periodogram. Third, the periodogram of the windowed segments is calculated. Fourth, the power spectrum is estimated using the average of these periodograms. These procedures effectively reduce the variance of the power spectrum estimation [*Welch*, 1967].

Parametric methods are those in which a signal is assumed to be an output of a linear system driven by white noise. There are several such methods including the Yule-Walker and Burg methods. By using an AR model to hypothetically "generate" the signal, Burg's method estimates the power spectrum from the parameters of the model [*Burg,* 1968]. The Burg method is used in this dissertation for the advantages of producing high frequency resolution and a stable AR model [*Proakis and Manolakis,* 1996]. The power spectrums estimated from both the Burg method and Welch's method are compared in this dissertation.

2.1.3.2 Digital filters

The second category of signal processing is digital filters. A filter is an operator and can be described in both the time and frequency domains. This section discusses the linear time-invariant filters from the frequency domain. A good discussion of filter design can be found in *Proakis and Manolakis* [1996].

The advantage of using digital filters is shown through convolution. Let $x(n)$ be the input signal to be filtered and $h(n)$ be the impulse response of the filter. The resulting signal $y(n)$ is expressed by the convolution between $x(n)$ and $h(n)$ as shown in Equation 2.14. With the Fourier/Z transform applied to equations, the convolution can be simplified as a product between the input and the filter, as shown in Equation 2.15. The output $Y(z)$ with desired frequency characteristics can be obtained by carefully designing a frequency-selective filter $H(z)$.

$$y(n) = \sum_{m} h(m)x(n-m) \tag{2.14}$$

$$Y(z) = H(z) \bullet X(z) \tag{2.15}$$

The filters can be categorized into two basic groups from Equation (2.14): finite impulse response (FIR) filters, which have the summation performed over a finite number of terms, and infinite impulse response (IIR) filters, which have the summation over an infinite number of terms. In real filter design, the IIR filters are often a recursive type with a feedback loop from the output to the input. An IIR can be defined as

$$Y(z) = \frac{\sum_{k=0}^{q} b_k z^{-k}}{1 + \sum_{k=1}^{p} a_k z^{-k}} \bullet X(z) \tag{2.16}$$

where p and q are integers, and a_k and b_k are the coefficients. Equation (2.16) represents a FIR filter if $a_k = 0$ for all k.

For a frequency-selective filter (IIR or FIR), the desired filter characteristics are specified in terms of the desired magnitude and phase response of the filter in the frequency domain. The details of FIR and IIR filter design are found in many books [for example, *Oppenheim et al.,* 1989; *Duhamel et al.,* 1990; *Proakis and Manolakis*, 1996]. In this dissertation, a notch filter is used to remove a specific frequency from a signal. The expression for a notch filter is shown below

$$H(z) = b_0 \frac{1 - \cos\varpi_0 z^{-1} + z^{-2}}{1 - 2r\cos\varpi_0 z^{-1} + r^2 z^{-2}} \tag{2.17}$$

where ϖ_0 is the desired frequency to remove and r is the notch coefficient. The notch filter is an IIR filter. With r well chosen, this filter can attenuate the magnitudes of a frequency without affecting other frequencies significantly. The magnitude response of a notch filter is shown in Figure 2.

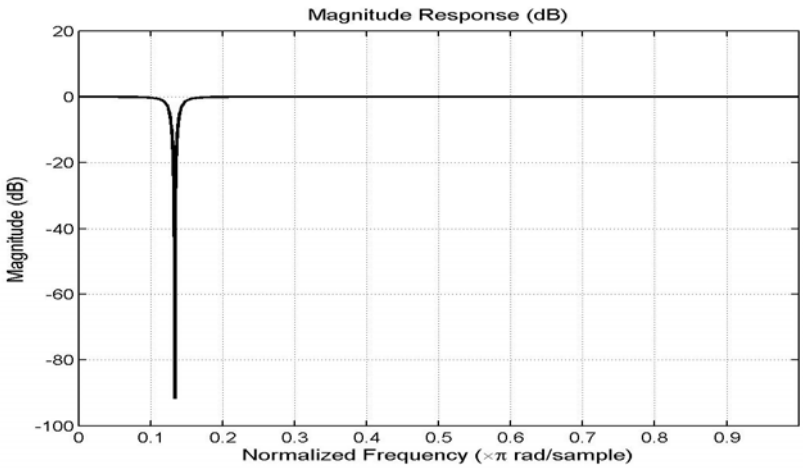

Figure 2. Frequency response of a notch filter

2.1.3.3 Summary

The section introduced power spectral analysis and digital filters based on the Fourier transform. They provide important information about the signals from the frequency domain. These methods are applied in Chapter 3 and 4 where the detailed applications are presented.

2.1.4 Wavelet Methods

Wavelet methods are used to decompose a signal into components of different frequency resolutions. They have the advantage of combining the time and frequency domain in the data analysis. *Morlet et al.* [1982] was the first to discuss the idea of a wavelet. *Daubechie* [1988] developed a theory and algorithm for the generation of compactly supported orthonormal wavelets. Wavelet methods are often implemented by filter banks. *Smith and Barnwell* [1986]

first reported the existence of two channel filter banks, which permitted perfect reconstruction of an input signal. Formulations for analyzing M-channel filter banks were subsequently developed by *Smith and Barnwell* [1987], *Vetterli* [1986] and *Vaidyanathan* [1987]. This section presents a brief introduction to the wavelet transform and filter banks. Comprehensive reviews can be found in *Strang et al.,* [1996].

2.1.4.1 Definitions

A wavelet φ is a function of zero average where the square of φ integrates to unity, as shown in Equation 2.18 and 2.19. By scaling the wavelet φ by s and translating it by u, a family of time-frequency wavelets, $\varphi_{u,s}(t)$, are defined in Equation 2.20.

$$\int_{-\infty}^{+\infty} \varphi(t)dt = 0, \tag{2.18}$$

$$\int_{-\infty}^{+\infty} \varphi^2(t)dt = 1, \tag{2.19}$$

$$\varphi_{u,s}(t) = \frac{1}{\sqrt{s}}\varphi\left(\frac{t-u}{s}\right) \tag{2.20}$$

The wavelet transform of a signal x at a scale s and a position u is computed by correlating x with the wavelets (Equation 2.21). By using the discretely sampled wavelets,

$$Wf(u,s) = \int_{-\infty}^{+\infty} x(t)\frac{1}{\sqrt{s}}\varphi^*\left(\frac{t-u}{s}\right)dt \tag{2.21}$$

the *discrete wavelet transform* (DWT) is shown in Equation 2.22. The DWT is often applied in numerical analysis with the discrete scale $s = s_0^j$ and the discrete translation $u = nu_0 s_0^j$. If s_0=2, Equation 2.22 represent a 2-channel wavelet transform; otherwise, it represents a multi-channel

wavelet transform [*Strange et al.,* 1996]. The 3-channel wavelets are used in this dissertation and discussed in Chapter 5.

$$Wf(j,n) = \frac{1}{\sqrt{s_0{}^j}} \int_{-\infty}^{+\infty} x(t)\varphi^* \left(\frac{t - nu_0 s_0^j}{s_0^j} \right) dt \qquad s_0 > 0 \tag{2.22}$$

The wavelet transform can be related to the commonly used Fourier transform. The Fourier transform represents a weighted sum of exponentials at different frequencies, and the weight at each different frequency is the Fourier coefficients. Analogously, the wavelet transform is a weighted sum of scaled and translated mother wavelets. Therefore, a mother wavelet replaces the exponential and the scaling and translation replace the frequency shifting. The time-frequency (or scale) representations of a signal are realized by wavelet methods.

2.1.4.2 Multiresolution Analysis

Multiresolution Analysis (MRA) introduces the subspaces, denoted as V_j and W_j respectively, at each resolution $s_0{}^j$. The characteristics of the subspaces have been well established [*Suter,* 1997; *Strang et al.,* 1996]. Those characteristics allow the projection of a signal $x(t)$ on the subspace V_j (called the scaling subspace) to be the approximation of the signal at the resolution $s = s_0{}^{-j}$ and the projection of $x(t)$ on the subspace W_j (called the wavelet subspace) to be the detail of the signal at the same resolution. A scaling function ϕ can therefore be designed such that the convolution between x and ϕ represents the approximation of $x(t)$ at a resolution $s = s_0{}^{-j}$; a wavelet function φ can be designed such that the convolution between x and φ represents the detail of $x(t)$. As the resolution and translation change, the scaling

function $\phi_{j,k}$ and wavelet function $\varphi_{j,k}$ are dilated and translated as defined in Equation 2.23 and 2.24 respectively.

$$\phi_{j,k}(t) = \frac{1}{\sqrt{s_0^j}} \phi(\frac{1}{\sqrt{s_0^j}} t - k) \tag{2.23}$$

$$\varphi_{j,k}(t) = \frac{1}{\sqrt{s_0^j}} \varphi(\frac{1}{\sqrt{s_0^j}} t - k) \tag{2.24}$$

2.1.4.3 Filter Bank Implementation

The scaling function and wavelet function are essentially filters. The scaling function is a low-pass filter and the wavelet function is a high-pass/band-pass filter. An invertible filter bank (that is, a set of filters) was introduced by *Esteban and Galand* [1977], which decomposes a discrete signal $x(n)$ into two signals half of its size, using a filtering and sub-sampling procedure. This theory was further expanded and established for the realization of the wavelet transform by *Smith and Barnwell* [1986]. The detailed descriptions of wavelets and filter banks are given in *Strang et al.*, [1996].

The filter banks consist of analysis banks, down-samplers, up-samplers and synthesis banks. An example of an M-channel filter bank is shown in Figure 3. The analysis banks are used to decompose a signal and the synthesis banks to reconstruct the signal. Down-samplers and up-samplers are commonly used to change the resolutions. In the analysis banks the low-pass, high-pass and band-pass filters are designed to realize the scaling function and the wavelet function. Each stage of the filter banks is briefly introduced below.

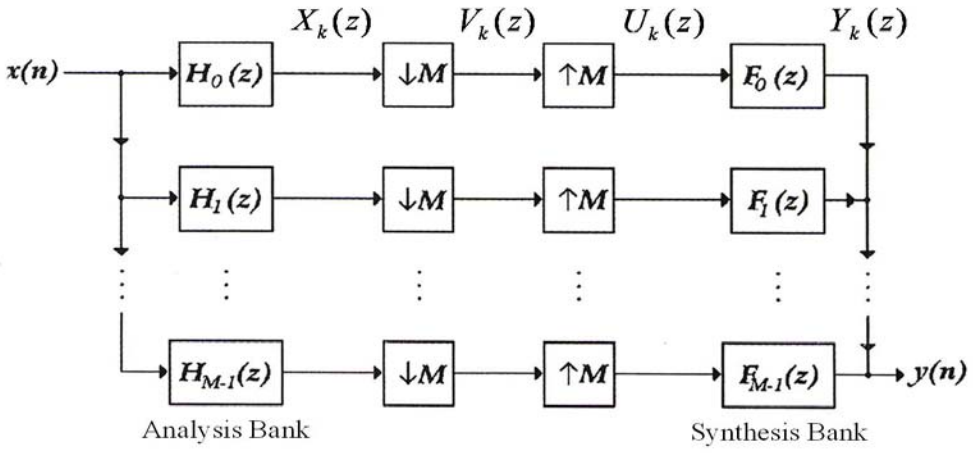

Figure 3. An M-band filter bank

(1) Analysis bank

The equation for the analysis stage is given by

$$X_k(z) = H_k(z)X(z) \tag{2.25}$$

where $H_k(z)$ are filters, $X(z)$ is the input signal, the $X_k(z)$ are the output and $k = 0,1,.....M-1$.

(2) Down-samplers

The M-channel down-samplers ($\downarrow M$) reserve only those samples that occurs at M-time multiples apart, as expressed in the equation below

$$V_k(z) = \frac{1}{M}\sum_{n=0}^{M-1} X_k(z^{-M}W_M^n) \tag{2.26}$$

where $W_M = \exp(\frac{-j2\pi}{M})$ is the M-th root of unity.

(3) Up-samplers

The M-channel up-samplers ($\uparrow M$) insert M-1 zeros between adjacent samples of the input signal, expressed as

$$U_k = V_k(z^M) \tag{2.27}$$

(4) Synthesis bank

The synthesis stage is represented by $Y(z) = \sum_{k=0}^{M-1} F_k(z) U_k(z)$ (2.28)

Combining these equations (2.25-2.28) together yields

$$\mathrm{Y}(z) = \frac{1}{M}\sum_{k=0}^{M-1} F_k(z)H_k(z)X(z) + \sum_{n=1}^{M-1}\frac{1}{M}\sum_{k=0}^{M-1} F_k(z)H_k(zW_M^n)X(zW_M^n) \tag{2.29}$$

The first part is the desired term that can be interpreted as the input signal weighted by the product of the analysis and synthesis filters; the second term is due to aliasing that can be set to zero. A perfect reconstruction system is a system free from aliasing. With properly designed scaling and wavelet filters, perfect reconstruction can be realized [*Strang et al.*, 1996].

2.1.4.4 A Harr wavelet

A simple Harr wavelet is presented here as an example. The Harr wavelet was first used by the Hungarian mathematician Alfréd Haar in 1910 and can be described as a step function

$$\varphi(t) = \begin{cases} -1\sqrt{2} & if\ -1 \le t \le 0 \\ 1/\sqrt{2} & 0 < t \le 1 \\ 0 & otherwise \end{cases} \tag{2.30}$$

The wavelet is in fact a difference between two points. A scaling function for this Harr wavelet is defined as

$$\phi(t) = \begin{cases} 1 & for\ 0 \le t < 1 \\ 0 & otherwise \end{cases} \tag{2.31}$$

The Harr wavelet has several advantages. First, it is much simpler compared to many complex wavelets. Second, the Haar wavelet transform can be considered to simply pair up input values, storing the difference and passing the sum. Therefore, the averages and differences, which are important for many physical signals, can be directly represented by the Harr wavelet. Third, it is orthonormal and can provide significant efficiency in signal decomposition and reconstruction. The 3-channel Harr wavelets are used to examine the data in Chapter 5.

2.1.4.5 Summary

This section introduced the wavelet transform and filter banks. Wavelet methods are powerful tools used to decompose a signal into components with different frequency resolutions, which provides significant details to understanding complex signals. Wavelet methods are used in Chapter 5.

2.2 Instruments and Measurements

This dissertation uses measurements from instruments on recent satellites, a digisonde, a GPS receiver and magnetometers, which are presented in sequence below.

2.2.1 TIMED Satellite

The NASA Thermosphere Ionosphere Mesosphere Energetics Dynamics (TIMED) spacecraft began normal operations on 22 January 2002 [*Woods et al.,* 1999, 2005]. One of the

TIMED's missions was to measure the solar soft X-rays and solar extreme ultraviolet (EUV) radiation using the Solar EUV Experiment (SEE) instrument. The SEE includes two instruments, EUV grating spectrograph (EGS) and XUV photometer system (XPS), which together measure the solar spectral irradiance from 0.1 to 193 nm.

The EGS is a normal incidence Rowland circle spectrograph with a spectral range of 27 to 193 nm. The EGS consists of one grating, one detector and two entrance slits. A blazed, mechanically ruled grating from Hyperfine is used in order to cover such a wide spectral range. A CODACON array detector, developed by G. M. Lawrence at the University of Colorado [*McClintock et al*., 1982], uses a microchannel plate (MCP) and coded anode electronics for its readout. The MCP is coated with Au that provides better dynamic range and serves as the photocathode; the electronics accumulate photon events into an image and read out the previous image simultaneously. The CODACON array detector can obtain a complete spectrum in a few seconds. The EGS has two entrance slits, each being 25 mm wide by 1 mm tall and offset 3 mm vertically from each other, are used to illuminate the detector. The EGS can measure the solar spectral range of EUV and FUV.

The XPS includes nine silicon XUV photodiodes and measures the solar irradiance from 0.1 to 27 nm. Each photodiode has one thin film filter deposited directly on the photodiode to avoid using metal foil filters, which are more difficult to handle, prone to develop pin holes, and degrade with time. Several materials are suitable for use as XUV filters for this wavelength range (0.1-27 nm) and the detail are given in *Powell et al.,* [1990] and *Woods et al.,* [2005]. For each XPS photodiode, the electronics are simple and include only a current amplifier and a voltage-to-frequency converter (VFC) that can read out the data.

The solar irradiance measurements from the SEE were retrieved from the website http://see.colorado.edu/see/. The data used in this dissertation (Chapter 3 and 4) include both the daily averages with flares removed and those from individual orbits (~ 97 minutes period) with solar flares included.

2.2.2 SNOE Satellite

The Solar X-ray Photometer (SXP) on the SNOE spacecraft performs photometric measurements of the solar soft X-ray irradiance from March 1998 [*Bailey et al.,* 2000, 2005]. The SNOE SXP uses the same techniques as SEE XPS, consisting of X-ray sensitive photodiodes with thin films deposited directly onto the active areas. The SNOE photodiodes have primary sensitivity in the spectral range of < 10 nm, 7 -17 nm and 17 - 20 nm respectively. Depending on the dates, the number of solar observations each day varied from 4 (for the earliest dates) to 16. The solar irradiance data are the daily averages without contributions from solar flares. The SNOE measurements are used in Chapter 3 and 4.

2.2.3 Digisonde

An ionosonde/digisonde is special radar for the examination of the ionosphere. Since the electron concentration and the refractive index of the ionosphere vary with height, the path of a radio wave is affected when it is traveling through the ionosphere. The refractive index is governed by the electron concentration, the magnetic field of the medium and the frequency of

the transmitted wave. By broadcasting a range of frequencies (usually 0.1-30MHz) and measuring the time it takes for each frequency to be reflected, it is possible to estimate the concentration and height of each layer of the ionosphere.

As the frequency increases, each wave is refracted less by the ionization in the layer, and penetrates the layer before it is reflected. The frequency at which a wave just penetrates a layer is called the critical frequency of that layer. The critical frequency is related to the electron densities by a simple relation:

$$\text{Critical frequency} = 8.98 \times \sqrt{Ne} \qquad (2.32)$$

where Ne is the electron density (the number of electrons per cubic meter). All transmitted frequencies above this critical frequency will penetrate this layer without reflection.

The digisondes have been widely used due to their advantages over the traditional ionosondes. The University of Massachusetts Lowell's Center for Atmospheric Research (UMLCAR) has produced a low power DigisondeTM Portable Sounder (DPS). The system compensates for a low power transmitter (300 W) by employing intrapulse coding, digital pulse compression and Doppler integration [*Reinisch,* 1988]. The data acquisition, control, signal processing, display and automatic data analysis have been condensed into a single multi-processor computer system. This is much more advanced than the traditional ionosonde which needs more power and has bigger size. The critical frequency of the F2 layer (foF2) measurements from a digisonde located at the Jicamarca Radio Observatory, Jicamarca, Peru are used in Chapters 4 and 5.

2.2.4 GPS Receiver

Recently GPS receivers have been used to measure the TEC, which is an integrated electron density measurement with contributions from the ionospheric D, E, F and topside regions. The GPS receiver near Ancon, Peru (-77.15° longitude, -11.78° latitude, 1.47 degrees geomagnetic latitude) measures the equatorial TEC [*Valladares et al.,* 2001] and provide important data for the low latitude ionosphere study. The GPS receiver obtains the data transmitted from GPS satellites. The ionospheric pierce point (i.e., the altitude at which the line of sight from the GPS satellite to the receiver intersects the peak of the F layer) is assumed to be 350 km. Possible errors from peak altitude variations are minimized by the use of near zenith observations in this analysis. The hourly averaged TEC measurements are used in Chapters 3, 4 and 5.

2.2.5 Magnetometer

A magnetometer is an instrument used to measure the strength and direction of the magnetic field in the vicinity of the instrument. It produces a graphic presentation of magnetic field variation. The magnetic field perturbations are usually resolved along a geomagnetically north-south (positive north), east-west (positive east), and vertical (positive down) direction, denoted as H, D, and Z components respectively. Geomagnetic indices data are used to describe the magnetic activity, or some of its components, at a planetary scale. A good description of the indices can be found in *Mayaud* [1980]. A brief introduction of the indices is presented below.

The *K indices* range in 28 steps from 0 (quiet) to 9 (greatly disturbed) with fractional parts expressed in thirds of a unit. The arithmetic mean of the K values scaled at the 13

observatories gives Kp. (These 13 stations are Lerwick (UK), Eskdalemuir (UK), Hartland (UK), Ottawa (Canada), Fredericksburg (USA), Meannook (Canada), Sitka (USA), Eyrewell (New Zealand), Canberra (Aus- tralia), Lovo (Sweden), Brorfelde (Denmark), Wingst (Germany), and Niemegk (Germany).)

The *a index* is a 3-hourly "equivalent amplitude" index of local geomagnetic activity, which is related to the 3-hourly *K index* according to the following scale:

K = 0	1	2	3	4	5	6	7	8	9
a = 0	3	7	15	27	48	80	140	240	400

The *ap* represents an averaged planetary index derived from a set of Kp stations using the 3-hour *a* indices. The *A index* is a daily average of geomagnetic activity derived from the 3-hourly *a* indices. The *Ap index* is an averaged planetary index derived from a set of specific Kp stations using the *A indices.*

The Dst index is derived from hourly scaling of low-latitude horizontal magnetic variation. They show the effect of the westward flowing high altitude equatorial ring current, which causes the "main phase" depression worldwide in the H-component field during large magnetic storms. The units of the Dst index are nano-Teslas (nT). The Ap, ap and Dst indices are used in this dissertation.

2.3 Summary

This chapter presented the background knowledge of signal processing techniques and introduced the instruments used in the study. Time series analysis, digital signal processing and wavelet methods are applied to the space physics data in order to understand the relationships between the measurements.

CHAPTER THREE
TOTAL ELECTRON CONTENT (TEC) AND SOLAR IRRADIANCE

3.1 Introduction

The short-term relationship between equatorial TEC and solar irradiance is presented in this chapter. In the low latitude ionosphere solar soft X-ray and extreme ultraviolet (EUV) radiation are most responsible for the ionization. The ionospheric electron density and height are expected to increase linearly with solar activity [*Evans,* 1977; *Davies,* 1980; *McNamara and Smith,* 1982]. However, due to a lack of solar irradiance measurements, the direct dependence of the ionospheric density on the Sun's EUV and soft X-rays has been studied for only brief periods, primarily during solar flares [*e.g., Afraimovich*, 2001 and *Zhang and Xiao*, 2002]. There have been studies of their relationship using a proxy, the 10.7cm radio flux (F10.7), for the Sun's short wavelength emissions [e.g., *Jakowski et al.,* 1991; *Su et al.*, 1999; *Liu et al.*, 2003]. However, the expected linear relationship between ionospheric densities and F10.7 breaks down for high values of F10.7 [*Kane*, 1992; *Rishbeth*, 1993; *Balan et al.*, 1994]. *Balan et al.* [1994] show that the Total Electron Content (TEC) and F2-layer peak electron density (NmF2) increase nonlinearly with F10.7, due to a nonlinear relationship between F10.7 and the modeled solar EUV irradiance. Therefore, proxy based studies of ionospheric densities and solar variations are not completely reliable, and an examination using short wavelength solar irradiances is needed to improve our understanding of their relationship.

Recently, photometers on the Student Nitric Oxide Explorer (SNOE) satellite made daily measurements of the solar soft X-ray irradiances (2-20nm) [*Bailey and Woods et al*., 1999;

Bailey et al., 2000, 2005]. *Solomon et al.* [2001] studied the effects of these soft X-rays on the lower ionosphere (100-200 km) and found good agreement between observed electron density profiles and model predictions using the SNOE solar irradiances. While the 2-20nm irradiances from SNOE deposit most of their energy below the peak of the F region, irradiances of 20-40 nm are responsible for most of the ionization near the peak of the F region. Since these wavelength bands are adjacent, the electron densities may have some correlation with the irradiances observed by SNOE.

This chapter examines the short-term relationship ($\leq$ 27 days) of solar soft X-rays from SNOE with the Total Electron Content (TEC) from a GPS receiver near Ancon, Peru. These comparisons indicate that there is a correlation between solar X-ray irradiances and TEC ($\leq$ 27 days), with X-rays leading TEC ~ 1day. Almost two years of solar irradiance and TEC measurements are used.

Four steps are used to determine the relationship between the X-rays and TEC. (1) The power spectral densities (PSDs) of the solar soft X-rays and TEC are calculated to show their temporal frequencies; and mathematical models are applied to find the frequencies of periodic variations in the signals. (2) Filters are used to remove distinct trends and extract periodic variations. The relationship between the 27-day variations in the TEC and X-rays is examined. (3) The remaining autocorrelations between the measurements in each series of data, indicated by the autocorrelation function at different time lags, are modeled and then removed using the model derived. After removal of the autocorrelations, the remaining signals for the TEC and X-rays pass statistical tests for white noise. (4) The cross-correlation functions (CCFs, the cross-correlation at different time lags) of the remaining TEC and X-ray signals are calculated to find the nonperiodic short-term relationship, and a model is deduced to describe this relationship.

3.2 Data

In this section, the soft X-ray irradiances from the SNOE satellite and TEC from Ancon, Peru are presented.

3.2.1 Solar Soft X- ray Irradiance Data

SNOE carried the solar X-ray photometer (SXP) which measured the solar soft X-ray irradiance in broad wavelength bands [*Bailey et al.*, 1999, 2000, 2005]. Measurements of three spectral ranges – approximately 2-7nm, 6-19nm, and 17-20nm – are used in the following analysis. These measurements began on 11 March 1998. The values used here are 'daily' values. Most of the following analysis uses data from 11 March 1998 to 23 August 1999 in order to avoid a gap of 39 days, beginning on 23 August 1999, in the TEC measurements. While interpolation can easily be used to fill small gaps, filling gaps longer than 27 days is more complicated and might significantly affect the results. Figure 4 (a) shows the solar irradiance measurements for the three spectral ranges from 11 March 1998 to 23 August 1999.

3.2.2 TEC Data

The TEC is an integrated electron density measurement with contributions from the ionospheric D, E, F and topside regions. Although the D and E regions contribute to the TEC, they are much narrower in height and are normally lower in density than the F region; consequently, their contributions to the TEC are less significant. At F region altitudes and higher,

variations in the production, loss and transport rates can be significant. Several factors affect the electron density and profile shape. The solar X-rays and extreme ultra-violet (EUV) are the most important sources of ions at equatorial latitudes. Neutral winds, neutral densities and ExB drift velocity, can also affect the electron density and profile shape. While the TEC is an integrated electron density measurement and will have a smaller response to changes in the profile shape than do the densities at a specific altitude, changes in the shape of the profile may affect the TEC due to the altitude dependence of ion lifetime.

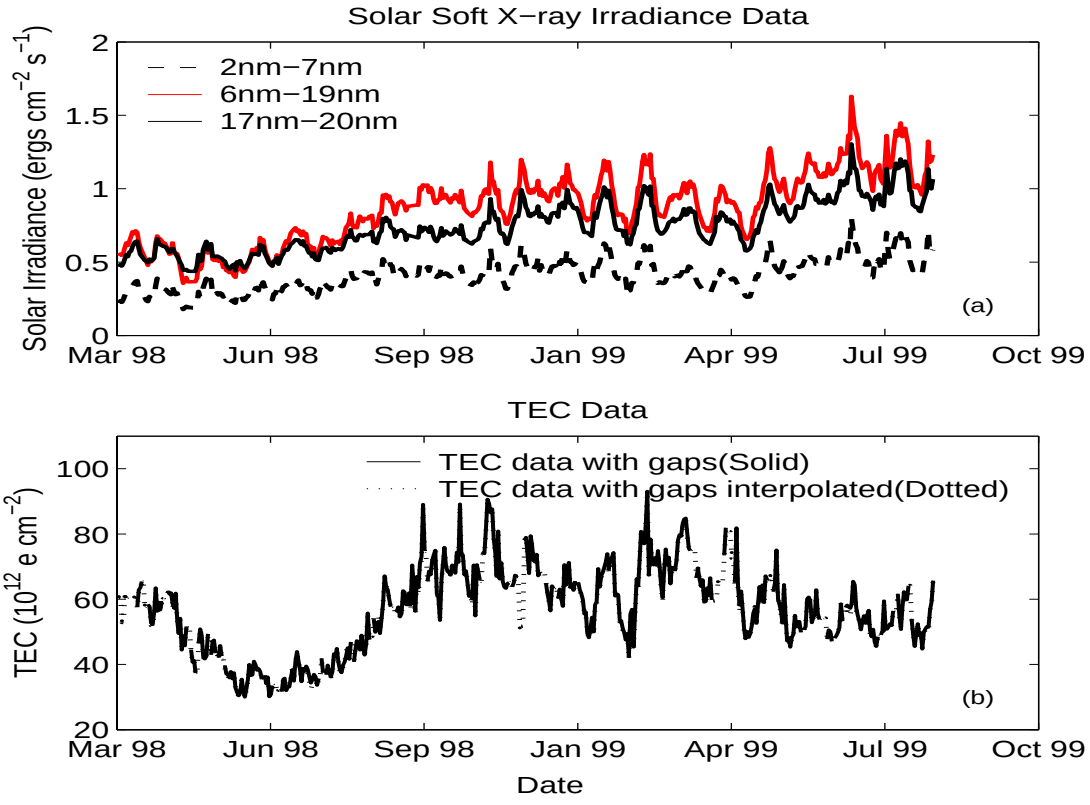

Figure 4. (a) Solar soft X-ray irradiances at noon UT measured at 2-7nm, 6-19nm and 17-20nm from 11 March 1998 to 23 August 1999. (b) Daily averaged noontime TEC from 11 March 1998 to 23 August 1999.

TEC data from a GPS receiver [*Valladares et al.,* 2001] near Ancon, Peru (-77.15° longitude, -11.78° latitude, 1.47 degrees geomagnetic latitude) are used in this study. Observations from 11 March 1998 to 23 August 1999 and from 2 October 1999 to 10 June 2000 are used in this study. For these dates the average TEC measurement was calculated for all observations whose ionospheric pierce point occurred within -12 ± 2 degrees latitude and -77 ± 2 degrees longitude and within the hour selected. Figure 4 (b) shows the averaged TEC from 12pm-1pm local time on 11 March 1998 to 23 August 1999. This figure shows that the TEC decreases between March 1998 to June 1998 and increases to October 1998; then decreases slightly between March 1999 and July 1999. This variation agrees with the seasonal anomaly, where the noon values of electron density are usually greater in winter than in summer. Seasonal changes in the neutral winds and neutral composition are the major causes for the anomaly. The shorter term variations in TEC will be compared with the X-ray irradiances in order to understand their relationship.

Gaps in the TEC data are filled using a cubic spline interpolation. The interpolated values are plotted in Figure 4 (b) with a dotted line. Although the number of interpolated values is relatively limited, the effects of this interpolation were tested using the X-ray flux measurements. For days when TEC data are missing, the solar irradiance measurements were replaced with interpolated values. Comparison of the power spectrum and the sample autocorrelation function (ACF) was made between flux data with and without interpolated values. This comparison showed that both had the same power spectral density; and the ACF showed no significant differences. Thus the linear properties of the solar irradiances were not changed by

the interpolation [*Kugiumtzis*, 1999], and it can be applied to the TEC without affecting the results.

3.3 Data analysis, Modeling and Transformations

Trends and periodic components are evident in both the X-rays and TEC (Figure 4 (a) (b)). These trends and periodic components need to be extracted in order to study the short-term relationships between these data. To isolate the trends and periodic components we take advantage of techniques developed for statistical time series analysis [e.g., *Brockwell and Davis,* 1996] and for signal processing [e.g., Orfanidis, 1996]. These techniques are realized with MATLAB, which has many of the basic routines needed.

3.3.1 Data Analysis

The trends and periodic components in the TEC and soft X-ray data are first studied by examining the power spectral density (PSD). Methods for PSD estimation can be categorized as either nonparametric or parametric [*Maple*, 1987]. Nonparametric methods are those in which the estimate of the PSD is based on calculating a fast Fourier transform (FFT) of the signal. The technique used here is Welch's averaged periodogram method, which consists of segmenting the data (50% overlap in this study), computing the Hanning-windowed FFT of each segment, and then averaging the PSD estimates. Shown in Figure 5 are the resulting power spectra from the TEC and the X-rays. Although the longer term - e.g., annual - variations derived from only 531 days of measurements are subject to uncertainty, these data are sufficient to estimate periods of <

27 days and to study the short-term relationship. In Figure 5 the largest peak in both the X-rays and TEC is at the lowest frequency (longest period) which indicates a long-term, approximately annual, variation. This long term variation will be subtracted from the signal later. The second largest peak represents a period of 25-27 days, which is approximately the solar rotation period.

To obtain a more accurate estimation of the temporal periods in the PSD a parametric method is used. This method first estimates the parameters (coefficients) of the linear model that hypothetically "generates" the signal; then finds the spectral estimation by studying the frequency response of the model. An Autoregressive (AR) model is assumed to generate the signal [*Maple*, 1987], and models with order less than 50 are sufficient for the spectral estimation. The roots of these polynomials are the poles in the complex plane. Since conjugate poles close to the unit circle (magnitude > 0.985) indicate periodic components in a signal, the periodic frequencies are found from the angles of the poles. The averaged frequency can be calculated as the order of the AR model is varied. This method indicates the TEC has a period of 25.6 ± 0.5 days; and X-ray irradiances have a period of 26.1 days with a similar uncertainty. These results are consistent with those from Welch's method. The periods seen in the TEC and X-ray irradiances are consistent with the observed solar rotation rates of 25 days (at the equator) to 31 days (at the poles) [*Schijver and Zwaan*, 2000].

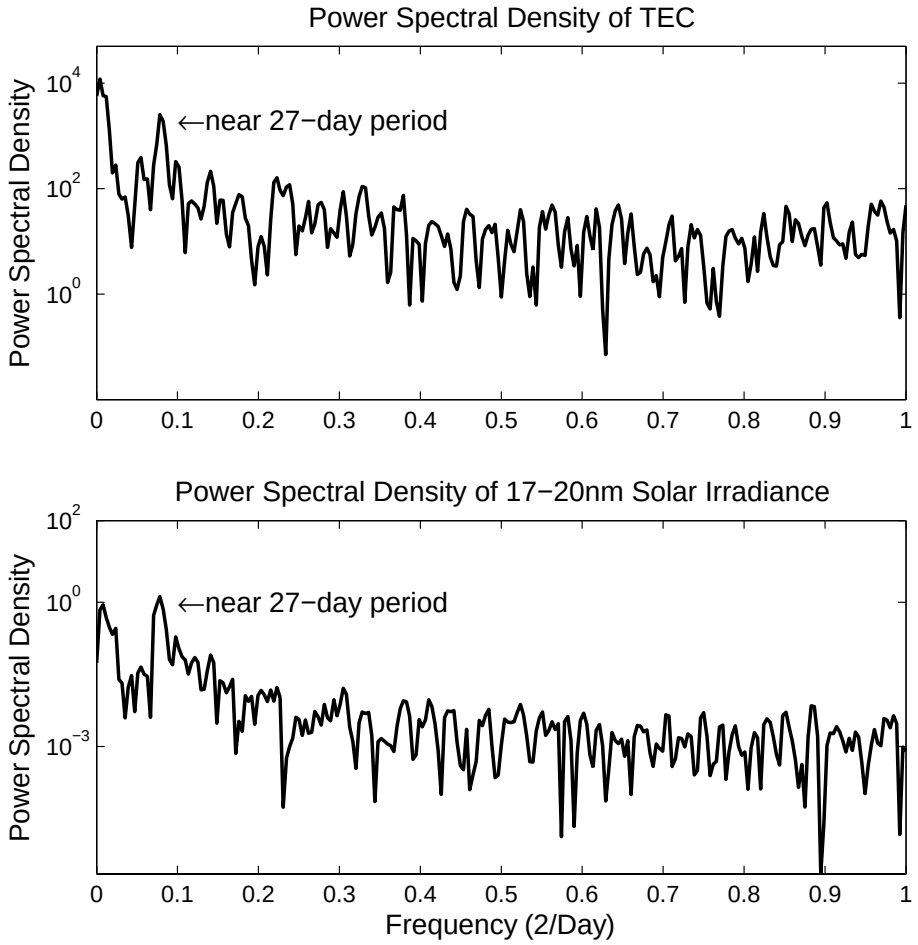

Figure 5. Power spectrum of the TEC and solar soft X-rays (17-20nm). The largest peak in both the X-rays and TEC indicates a long-term (> 27 day) variation. The second largest peak represents a periodic variation of approximately 27 days.

3.3.2 Modeling and Transformations

Removing the autocorrelations is an essential step in understanding the relationships between the TEC and soft X-ray observations. After the autocorrelations within each

measurement are removed, large values in the Cross-Correlation Function (CCF) indicate the existence of strong correlations between the measurements [e.g., *Brockwell and Davis*, 1996]. To remove the autocorrelations, each series is modeled individually as a function of the previous observations in the series. By subtracting the modeled series from that observed, the autocorrelations are removed, leaving residuals that are less correlated. Some transformations (changes of variable) are also used to make the data more suitable for modeling. The modeling is considered sufficient when the autocorrelation functions (ACFs) of the residuals for each series are consistent with white noise.

At each step of the analysis, correlations between measurements are examined. While simple correlations are sometimes used in these comparisons, rather than CCFs, the results are consistent to those obtained using a CCF (or equivalently time lags). Correlations for both X-ray irradiances and F10.7 are calculated to determine which has the higher correlation with TEC. Also, in order to better understand the effects of the modeling, the standard deviation of the TEC is calculated after each step. These standard deviations quantify the amount of variation modeled in each step.

The first transformation is to take the logarithm of the signals. Taking the logarithm is an effective, commonly used way to stabilize the variance when it changes significantly across the observations, as it does for these data. This change of variable also allows us to use a linear model, rather than a nonlinear one, to fit the data. After taking the logarithm, the mean TEC is 4.4 and the mean X-ray irradiances are -0.23, 0.51 and 0.37 respectively for the 2-7nm, 6-19nm and 17-20nm wavelength bands. The normalized cross-correlation coefficient between the X-ray irradiances and TEC without a time lag (i.e., correlation) is 0.5, significantly better than the

correlation of 0.3 between the F10.7 and TEC. The standard deviation of the TEC after taking the logarithm is 0.24.

Next, a 27-day moving average is subtracted from each signal. This moving average filter removes the trends and periods > 29 days while preserving components with periods ≤ 28 days. The signal removed includes annual and semiannual variations in the TEC. After subtracting the moving average, the correlation between the X-ray irradiances and TEC is 0.6, significantly higher than the 0.5 correlation between F10.7 and TEC, and the STD of the TEC is 0.1056, approximately 0.44 of the STD of the original signal. In Figure 3.3 the resulting 17-20nm solar irradiances and TEC are plotted. A similar relationship is seen between the other wavelength bands and TEC.

In Figure 6 a periodic component, 25.6 ± 0.5 days in the TEC and 26.1 ± 0.5 days in the X-rays, is clearly seen. Since the average period of 25.8 days is within the uncertainty of both measurements, a notch filter [Orfanidis, 1996] of 25.8 days is used on both. A notch filter is shown in the equation

$$H(z) = b_0 \frac{1 - \cos\varpi_0 z^{-1} + z^{-2}}{1 - 2r\cos\varpi_0 z^{-1} + r^2 z^{-2}} \tag{3.1}$$

Where ϖ_0 is the desired frequency to move, r is the notch coefficient. With r chose as 0.98, this filter can attenuate the magnitudes of either period by ~40DB; without affecting periods shorter than 23 days (the 3DB cut off frequency). The signals extracted by the filter are plotted in Figure 7, which is approximately 0.10 (i.e., 10%) of the original variation in the signal. Like many other filters, the notch filter initially responds to the input signal with oscillations and the extraction of the periodic components is not stable until it passes the settling time, i.e., the time when its performance becomes stable. Therefore, the first 100 points are excluded from the analysis in

order to avoid oscillations produced by the filter's impulse response. Figure 7 shows the extracted signals after omission of these points. A correlation of 0.9 was found between the extracted TEC and X-ray (17-20nm) signals, which is better than the correlation of 0.8 between TEC and F10.7.

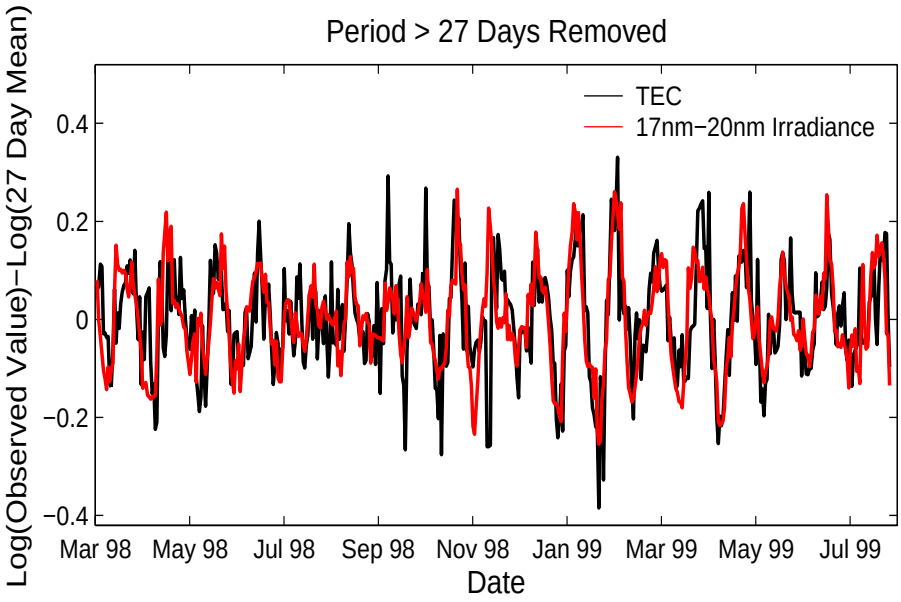

Figure 6. TEC and solar soft X-ray data after removal of the long-term (> 27 day period) variation. The figure indicates a significant relationship may exist between the short-term variations in the solar soft X-rays and TEC.

From Figure 7 it is clear that the TEC variations follow the X-ray irradiances. To determine the phase difference, correlations for different time delays were calculated. The highest correlations occur with the 1 and 2-day delayed X-ray irradiances, suggesting a 1.5-day difference. In an attempt to increase the temporal resolution, values were interpolated for times at

half the original interval. Correlations calculated using these interpolated values suggest smaller phase difference, i.e., ~1 day. One should also take differences in observation times into account. The X-ray irradiances are calculated for noon universal time each day; therefore, they precede the TEC measurements by approximately 5 hours (0.21 days). Consequently, a more accurate phase difference is 0.8-1.3 days, indicating the X-ray irradiances from the previous days affect the TEC significantly. Although the phase difference varies with time in Figure 7, the differences are not statistically significant and the approximately 1-day delay consistently appears when using subsets of these data.

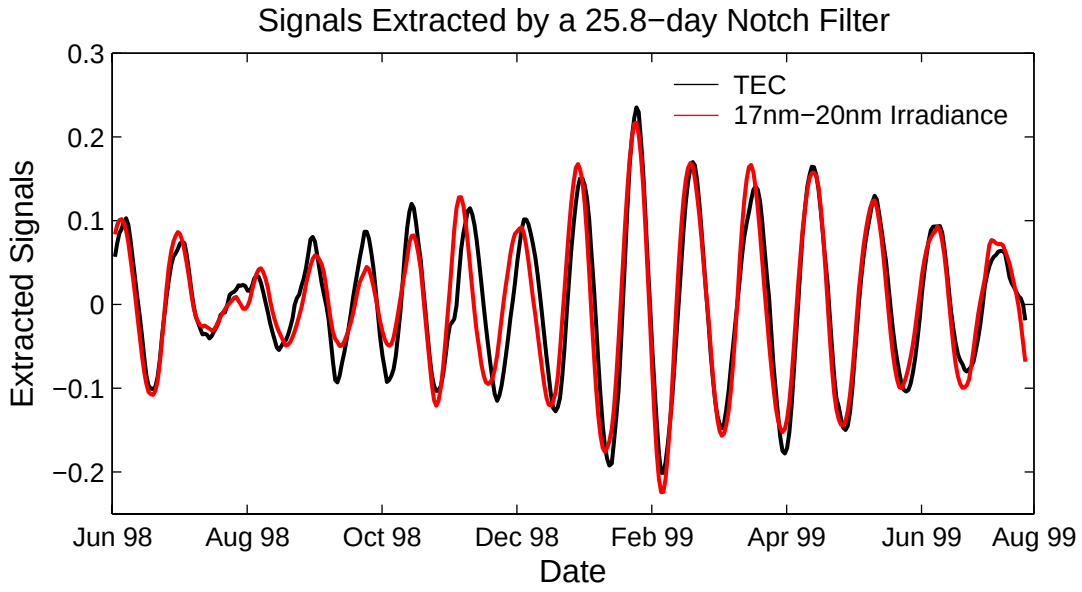

Figure 7. TEC and solar soft X-ray signals extracted from the data shown in Figure 3 using a 25.8 day notch filter. The figure shows there is a ~ 1 day phase difference between the solar soft X-rays and TEC, with the X-rays leading TEC.

This phase difference is similar to that seen between changes in the soft X-rays and the neutral density. *Eastes et al.* [2004] found the two are well correlated (see their Figure 2) with changes in the X-rays leading those in the neutral density by approximately 1.5 days. Therefore, the phase difference between the X-rays and TEC is consistent with neutral densities affecting the TEC. An ionospheric response to neutral density variations is also be consistent with previous studies [*Richards et al.,* 1994; *Richards,* 2002; *Fuller-Rowell,* 1997], but the measurements used here do not provide direct evidence that the neutral densities are responsible. Since the ~27 day variation is approximately 0.10 of the total variation in TEC, the ~27 day variations in neutral density may be responsible for 0.10 of the total change in TEC.

Next, the difference between successive days is taken. This removes any remaining variations with periods longer than one day, and the resulting series are stationary, i.e., the mean and the variance are not changing with time. The ACF of the differenced signals indicates the existence of autocorrelations. In this case the autocorrelations in both the X-ray irradiances and the TEC can be represented by a Moving Average (MA) model [e.g., *Brockwell and Davis*, 1996]. To remove the autocorrelations the best fit MA model is subtracted from the original signal. The whiteness of the residuals is demonstrated by the sample ACF which is plotted in Figure 8. True white noise has zero mean and auto covariance within the 95% confidence levels at lags other than 0, which is satisfied as shown in Figure 8. The remaining signals are therefore said to be 'prewhitened'. The residual TEC contains approximately 0.28 of the original variation in the TEC. The cross-correlation with the prewhitened X-ray irradiances is studied below.

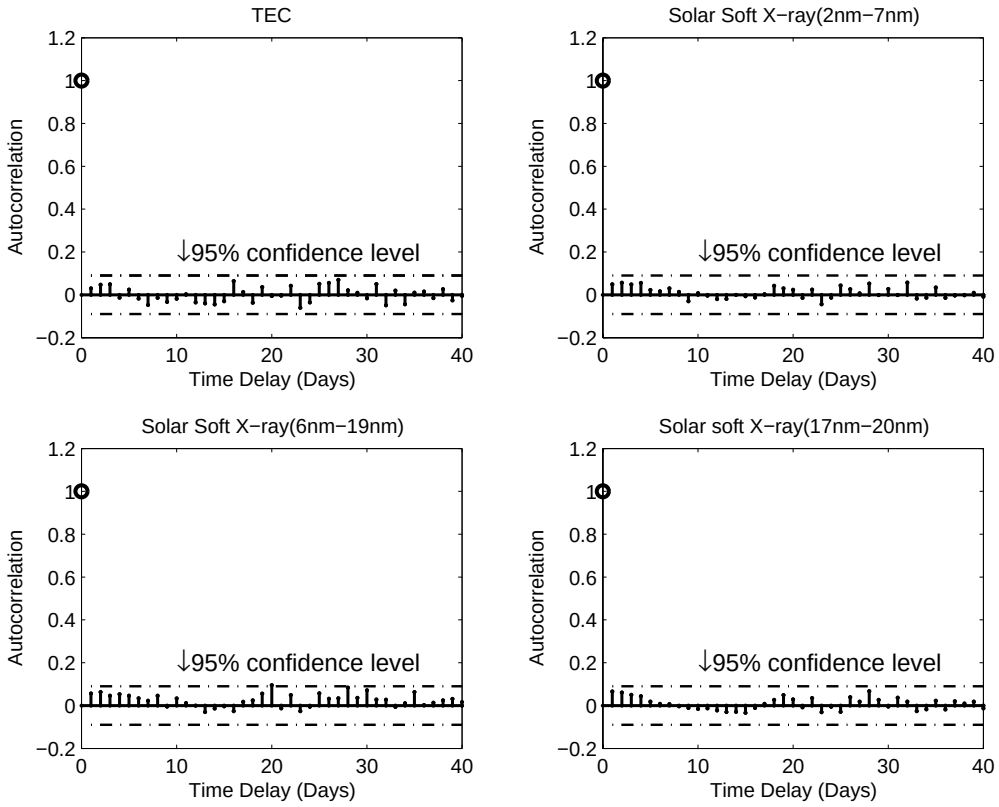

Figure 8. Autocorrelation function (ACF) of the TEC and solar soft X-rays after prewhitening (i.e., removal of the autocorrelations). As seen by the correlation of the observation with itself (a time delay of 0 days), 1.0 represents perfect correlation.

3.4 Cross-Correlation Function (CCF) Analysis

The CCF gives cross-correlations at different time lags, and it can be used to study the relationship between X-ray irradiances and TEC. Figure 9 shows the CCF of the X-ray irradiances and TEC after prewhitening. The TEC is clearly correlated with X-ray irradiances

from previous days but not with the X-rays on the day when the TEC is measured. The TEC has a correlation of 0.2 with both the 1-day and 2-day delayed X-ray irradiances, which is a factor of 2.5 greater than the 95% confidence level of 0.087. Figure 9 also shows a 0.15 correlation between TEC and the 3-day delayed X-ray irradiances at 6-19nm and 17-20nm, but not at 2-7nm. This decrease in correlation at 2-7nm is consistent with the neutral densities being less dependent on these wavelengths. Therefore, the total correlation between the X-rays (either 6-19nm or 17-20nm) and TEC is approximately 0.5 (0.3 above the noise level when combined in quadrature) since the autocorrelations between the X-ray irradiance measurements have been removed through the prewhitening process discussed earlier.

The 0.5 correlation between the X-ray irradiances and TEC (delayed 1, 2, and 3 days) suggests a relationship exists between these measurements. In comparison, the correlation between F10.7 and TEC after prewhitening was at or below the noise level (0.087in this case) for all time lags. Therefore, TEC has a clearer and more significant relationship with X-ray irradiances than with F10.7.

The prewhitened TEC is 0.28 (i.e., 28%) of the original variation in TEC, and has a 0.5 correlation (0.3 above the noise) with the X-ray irradiances. Therefore, X-ray irradiances should account for 0.08 (i.e., 0.28×0.3) of the total variation in TEC. As with the 27 day periodic variations, the X-rays lead the TEC and this is consistent with the effects of neutral density as discussed earlier.

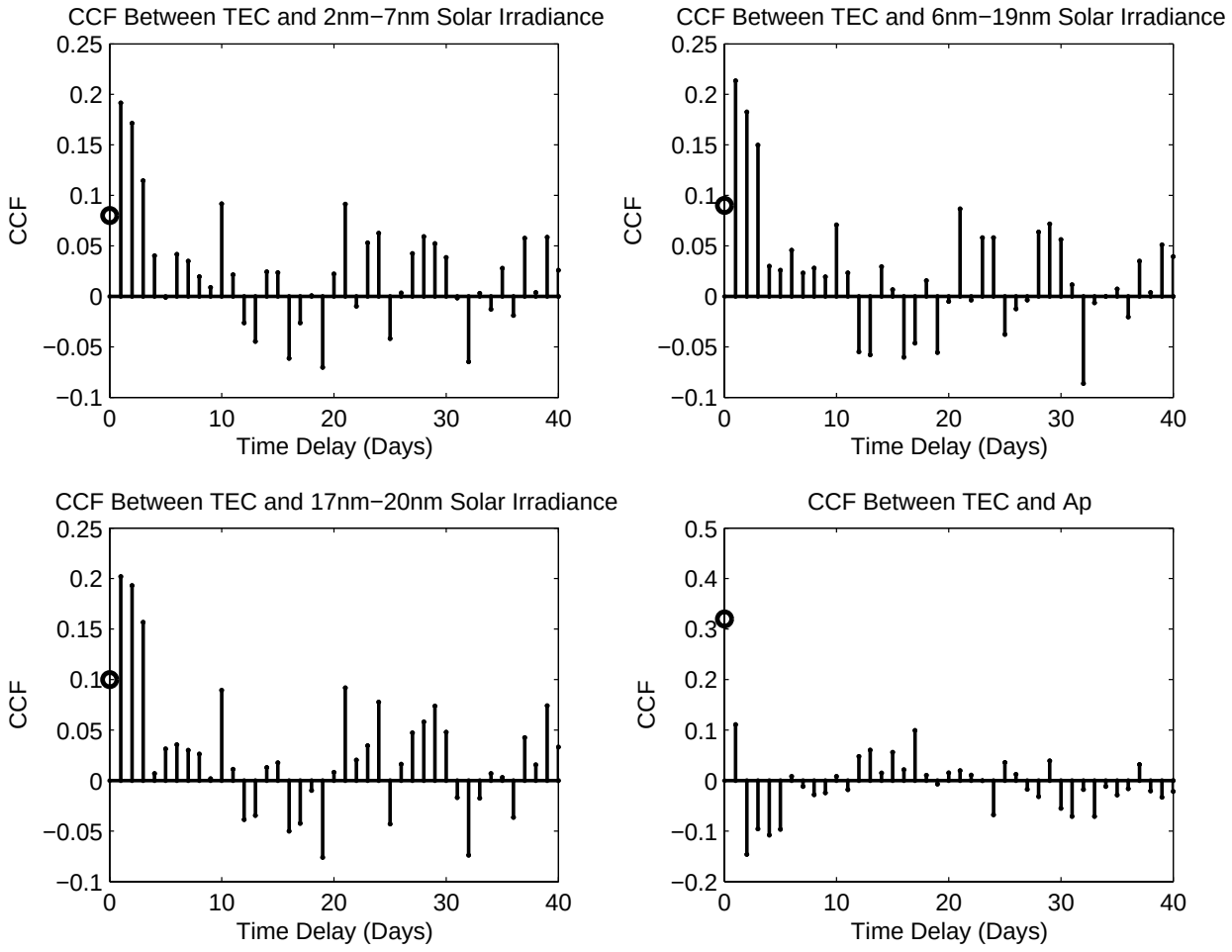

Figure 9. Cross-correlation of the TEC with the solar soft X-rays and Ap after prewhitening. These values indicate significant correlations between the TEC and the X-ray irradiances on the previous 1-3 days still exist.

Ionospheric densities are also expected to have a prompt response to changes in the solar short wavelength irradiances. This behavior has been seen following solar flares [e.g., *Zhang and Xiao*, 2002; *Thomason, et al.,* 2004; *Tsurutani et al.,* 2005], but a significant dependence on the solar irradiance from the same day is not seen in this analysis. The one-hour averaged TEC measurements may be responsible for the lack of dependence on solar irradiances from the same

day. Ion lifetimes are less than an hour in the F region. In order to see the response of ionospheric densities to concurrent changes in the X-ray irradiances, higher temporal resolution is apparently necessary for the ionospheric and solar data.

3.5 Modeling

In the analysis presented above, individual bands of soft X-rays are used, but since the three bands are not completely correlated, there is a possibility that the other bands contain additional information that could be used to provide a more accurate relationship between the TEC and soft X-rays. The three bands are highly correlated, with cross-correlation coefficients of 0.90-0.94. Therefore, the three signals are first orthogonalized to avoid redundancy problems before attempting to use all three to model TEC. Fits obtained when using three bands are not significantly better than those using only one, with the initial wavelength band, to which the other two are orthogonalized being the most significant. Thus each band appears to provide similar information, and only one band will be used in the analysis below.

Least square fits to the TEC were calculated. Using the 17-20nm irradiances after prewhitening as an example, the best fit to the TEC is given by

$$TEC_t = a_1 \cdot Solar_{t-1} + a_2 \cdot Solar_{t-2} + a_3 \cdot Solar_{t-3} \qquad (3.2)$$

where $Solar_{t-1}, Solar_{t-2}, Solar_{t-3}$ are 1, 2, 3-day delayed solar soft X-ray irradiances in 17-20nm, a_1, a_2, a_3 are the model coefficients, and TEC_t is the modeled TEC for the present day. The results are shown in Table 3.1.The magnitudes of the coefficients are consistent with CCF analysis. This model represents approximately 0.3 (i.e., 30%) of the variation in the prewhitened

TEC, which is consistent with the amount of signal above the noise level (see [24]). Since the remaining TEC is approximately 0.28 of the original variation (see [21] and [24]); therefore, the model based on soft X-rays represents 0.08 (i.e., 0.28×0.3) of the original variation in TEC. This non-periodic correlation of the TEC with the X-rays is almost as large as that from the 27 day period, which accounted for 0.10 of the total variation seen in TEC. Combining the 27 day (periodic) variation and the non-periodic short term variations indicates the X-ray irradiances can account for 0.18 of the change in TEC. The model produces a Final Prediction Error (FPE) of 0.0022.

Table 1. Coefficients for modeling TEC from solar soft X-rays (17-20nm)

	Solar Irradiance (17-20nm)		
Time delay (days)	1	2	3
Model coefficients	0.3	0.24	0.17

The effect of geomagnetic activity, as indicated by Ap, on TEC was also studied. Ap accounts for 0.1 of the variation in TEC. Thus the variations in the X-ray flux are responsible for almost twice as much TEC variation as Ap.

3.6 Discussion

Measurements from a second time period, 2 October 1999 to 10 June 2000, are used to test the model. As for the 11 March 1998-23 August 1999 data presented previously, values are interpolated for the small gaps. Figure 10 show the X-ray irradiance and TEC measurements. As for the previous data, X-ray irradiances have a higher correlation with TEC than F10.7 does. Applying the model presented earlier to this additional set of data gives a FPE of 0.0023, not significantly different from the FPE of 0.0022 obtained previously.

Another possible reason for the lack of same day correlation between TEC and SNOE measurements of solar irradiance is that most of the solar photons measured by SNOE are absorbed at altitudes below the F region. To address this possibility, longer wavelength solar irradiances from the Solar EUV Experiment (SEE) and TEC were examined. The 20-40nm and 20-193nm solar irradiances from 9 February 2002 to 31 December 2002 were used. Comparison of the TEC with 20-40nm, 20-193nm and F10.7 data are displayed in Figure 11. Correlations of 0.78, 0.5 and 0.33 are found respectively between TEC and the 20-193nm irradiances, the 20-40nm irradiance and F10.7. The TEC is more significantly correlated with solar irradiance measurements than with F10.7. EUV wavelengths > 40nm affect the long term ionospheric variations more significantly than shorter wavelength bands, and they have a more prompt effect on TEC. However, the short-term relationship of these EUV irradiances with TEC ($\leq$27 days) shown is based on only the 100 days of data remaining after applying the notch filter and excluding the first 100 points.

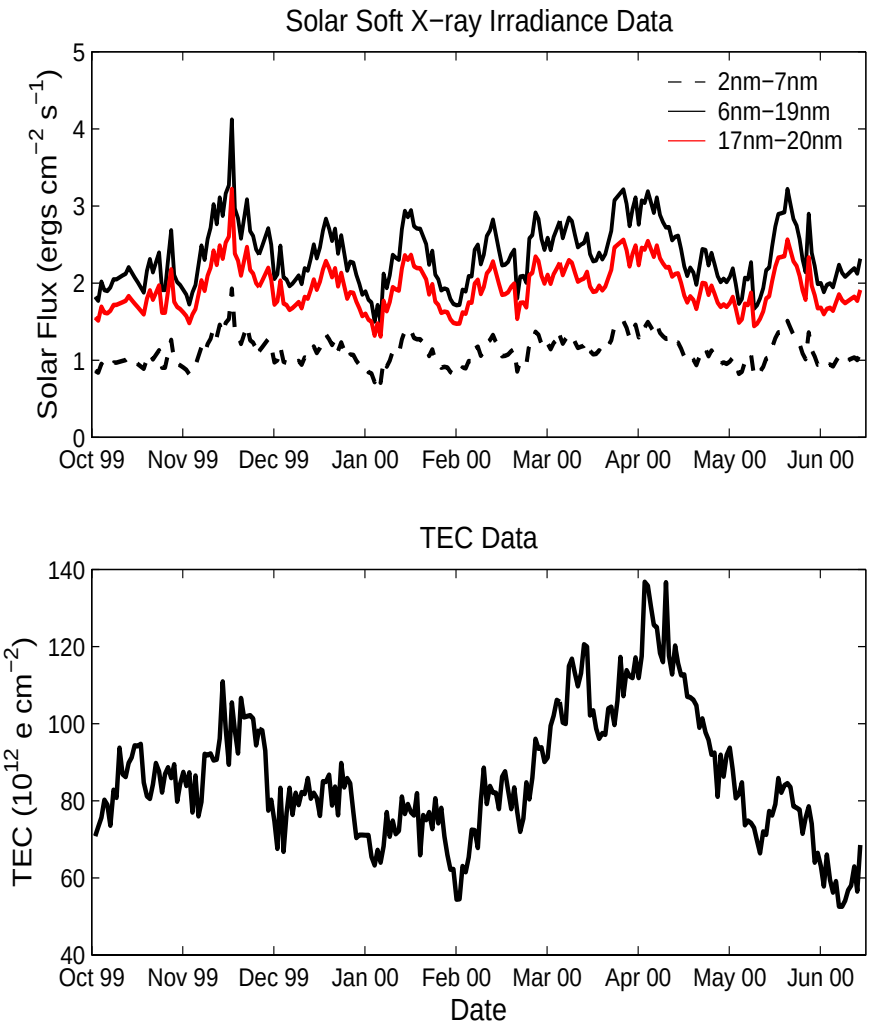

Figure 10. Solar soft X-rays at noon UT measured at 2-7nm, 6-19nm and 17-20nm from 2 October 1999 to 10 June 2000 (top). Daily averaged noontime TEC from 2 October 1999 to 10 June 2000 (bottom).

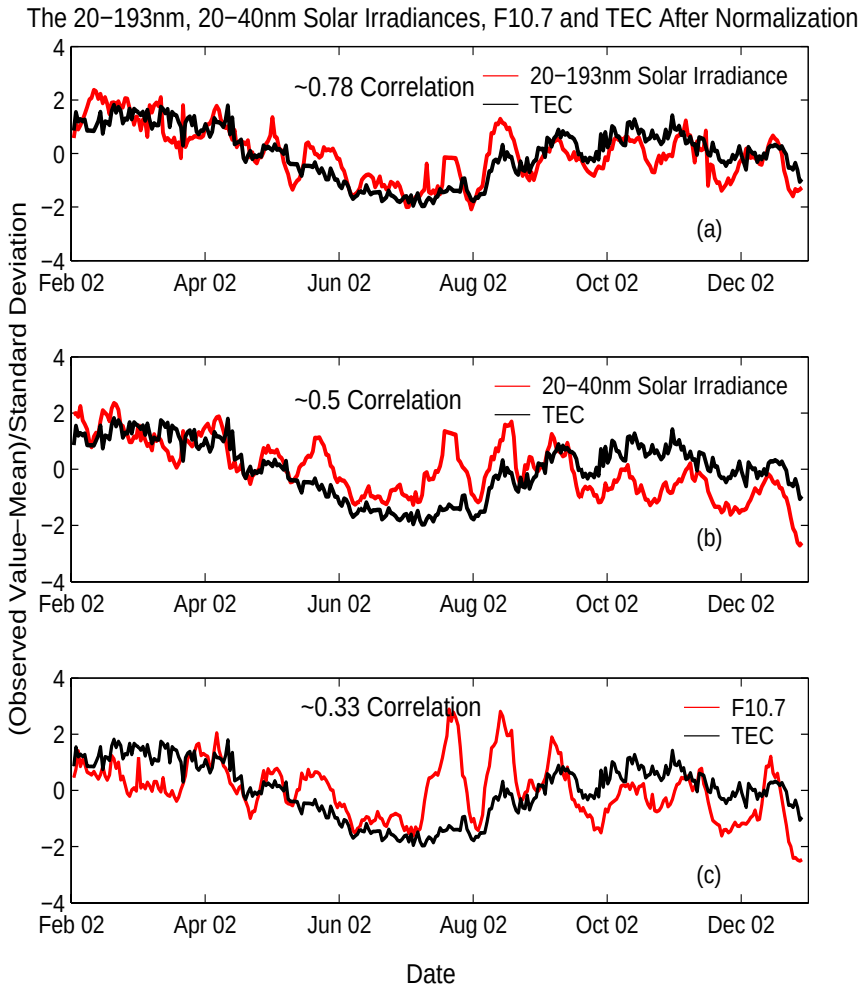

Figure 11. Solar Irradiances (20-193nm, 20-40nm), F10.7 and TEC from 8 February 2002 to 31 December 2002 after normalization.

3.7 Summary

Comparisons of the solar soft X-ray irradiances from the SNOE satellite and equatorial TEC from 1998 to 1999 show X-ray irradiances allow significantly better prediction of TEC than F10.7. A correlation of 0.5 appears between the original X-ray irradiances and TEC, compared to 0.3 between F10.7 and TEC; and a 0.6 correlation is seen after removing long term variations

(i.e., ≤ 27 day period remained), compared to 0.5 for F10.7 and TEC. In the shorter-term, non-periodic variations (the signal remaining after prewhitening) a 0.3 correlation between the X-rays and TEC was found, in contrast, no meaningful correlation of F10.7 is seen with TEC after prewhitening. This means the X-ray irradiances can represent 0.08 (i.e., 8%) more of the TEC variation than F10.7 can.

The comparisons of the short term variations in the X-ray irradiances and TEC show that the TEC depends strongly on the previous 2-3 days of X-ray irradiances and that the X-rays lead TEC by 0.8-1.3 days. This phase difference is consistent with that seen between the neutral densities and soft X-ray irradiances, which suggest that this effect might be associated with neutral density changes. Based on this attribution, neutral density changes would be responsible for short-term (27 days or less) TEC changes of approximately 0.18 of the total TEC.

CHAPTER FOUR
PEAK ELECTRON DENSITY AND SOLAR IRRADIANCE

4.1 Introduction

This chapter discusses the dependence of peak electron density on solar irradiance. *Forbes et al.,* [2000] evaluated the observed ionospheric variability and attributed it to a number of sources such as solar ionizing flux, solar wind conditions and propagating waves– gravity waves, tides, and planetary waves. The contributions from different sources were also studied in more recent work [*Mendillo et al.,* 2002; *Altadill et al.,* 2003; *Lastovicka et al.,* 2003; *Pancheva et al.,* 2004; *Fagundes et al.,* 2005]. Most of these studies focused on the effects of geomagnetic and planetary waves; and the contribution of solar irradiances was studied using the F10.7 radio flux as a proxy for the solar extreme ultraviolet (EUV). Although the solar EUV produces most of the ionization in the F region, their results indicated an insignificant solar effect on the short-term variations of ionospheric densities. Use of F10.7 as a proxy for the EUV in the previous studies may have significantly affected the results.

Direct measurements of solar irradiances are available from recent satellites. The SNOE satellite began measuring solar soft X-ray irradiances (0.1 nm-20 nm) in March 1998 [*Bailey et al*., 2000; *Bailey et al*., 2005]. More recently, the TIMED satellite has measured the solar spectral irradiance (0.1 nm-193 nm) in the X-ray ultraviolet (XUV), extreme ultraviolet (EUV), and far ultraviolet (FUV) ranges from February 2002 to present [*Woods et al.,* 2005]. These direct measurements of Sun's short wavelength emissions should enable us to better understand the effect of solar irradiances on the short-term variations of ionosphere, compared to

proxies such as F10.7 [*Kane*, 1992; *Rishbeth*, 1993; *Balan et al.,* 1994; *Wang et al.,* 2006].

Recent analysis of ionospheric electron density data and SNOE data, by *Wang et al.* [2006] found clear short-term ($\leq$ 27 days) correlations (~0.6) between total electron content (TEC) and solar irradiances. Their results indicate that the short-term variations in ionospheric densities have a more significant correlation with short wavelength solar irradiances than expected from studies using F10.7. In order to advance the understanding of solar effects on ionospheric variations, the relationship between peak electron densities and solar irradiances (X-rays and EUV) is examined in this study. As a measure of the peak electron densities, the critical frequencies of the F2 layer (foF2) from Jicamarca, Peru are used.

This chapter is organized in the following sequence: (1) data description; (2) data analysis and comparison of the short-term correlations between solar irradiances and foF2 as a function of local time; (3) discussion of how the periodic variations in foF2 change with local time; (4) conclusions.

4.2 Data

Short wavelength solar irradiances from SNOE and TIMED are used in this study. The SNOE measurements are from two bands – approximately 6-19 nm and 17-20 nm. Solar irradiances of 0.1-7 nm are not used because they had smaller correlations with TEC than the 6-19 nm and 17-20 nm bands [*Wang et al.,* 2006]. Measurements from11 March 1998 through January 2000 were used. The values used, shown in Figure 12 (a), are 'daily' values.

The second set of solar data used in this study is from the Solar EUV Experiment (SEE) aboard the TIMED satellite. Descriptions of the SEE instruments are given in Chapter 2. The

solar irradiance measurements were retrieved from the SEE website http://see.colorado.edu/see/. Latest data versions, used in this study, includes both daily averages with flares removed and data from individual orbits (~ 97 minutes period) with solar flares included. The results presented here used short wavelength solar irradiances (6-19 nm and 17-20 nm for the X-rays, 27-39 nm for the EUV), both daily averages and individual orbits, from February 2002 to December 2004. When using data from individual orbits, flares were removed in order to be consistent with daily average data from TIMED and SNOE. The daily TIMED SEE measurements (6-19 nm, 17-20nm and 27-39 nm) are shown in Figure 12 (b).

The foF2 data are from a digisonde located at the Jicamarca Radio Observatory in Peru [*Reinisch,* 1996]. The vertical soundings of the ionosphere are normally obtained every ~30 minutes and were automatically scaled using the ARTIST inversion algorithm [*Reinisch et al.,* 1983]. These data are downloaded from http://umlcar.uml.edu/DIDBase/, provided by the Center for Atmospheric Research at the University of Massachusetts, Lowell. There are usually two measurements in an hour, and averages are calculated from the one nearest the hour and the one nearest the half hour. If additional measurements are available within the hour, they are included in the average. The hourly averages of foF2 from 0700 to 1900 LT are used from March 1998 to January 2000 and from February 2002 to December 2004. An example of these data, collected from 0800 to 0900 LT during 1998-2000 and 2002-2004 respectively, is shown in Figures 13 (a and b).

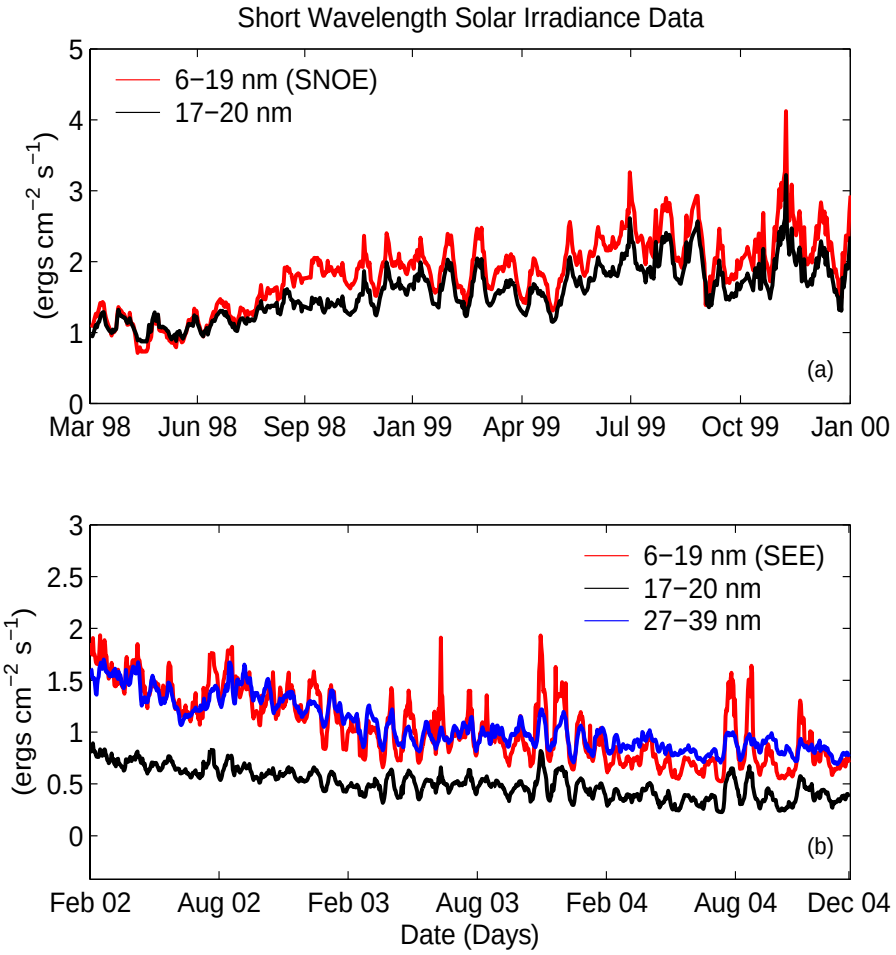

Figure 12. (a) The daily solar irradiance measured from SNOE (1998-2000). (b) The daily solar data from TIMED (2002-2004).

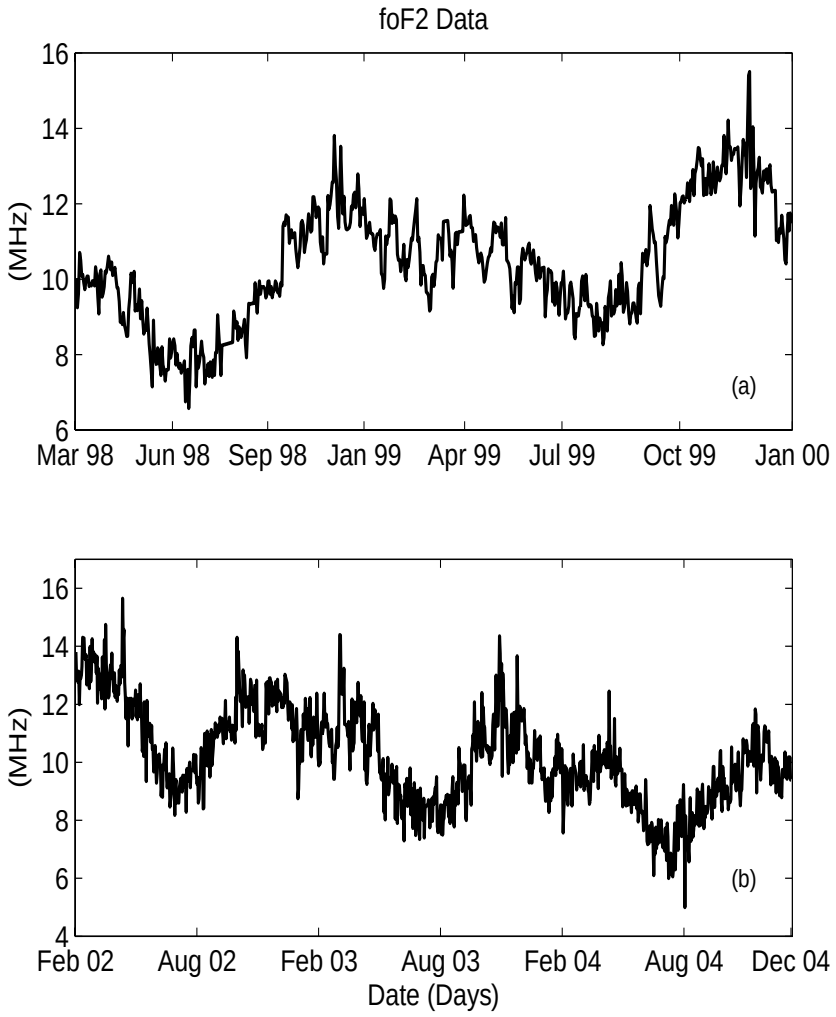

Figure 13. Averages of 0800-0900 LT measurements of foF2 from Jicamarca, Peru for (a) 1998-2000 and (b) 2002-2004.

4.3 Data Analysis and Correlation Discussion

In order to more easily study the short-term relationship, a 27-day moving average is removed from both the solar irradiances (both daily average and individual orbits) and hourly

foF2. The remaining signals, which will be referred to as the residuals, contain variations with periods of ≤ 27 days. The magnitude of the correlation between the residuals is a measure of the linear, short-term relationship between solar irradiances and foF2.

The correlations are similar when using solar irradiances from daily averages or individual orbits. An example, using daily solar irradiances and hourly foF2, is shown in Figure 14. It shows: (1) the foF2 has higher correlations with solar soft X-rays than with solar EUV; (2) correlations between foF2 and solar irradiances decrease from 0700 to 1900 LT; and (3) correlations in the afternoon are higher when using solar X-rays from SNOE than those from TIMED. Each of these three points will now be discussed in more detail.

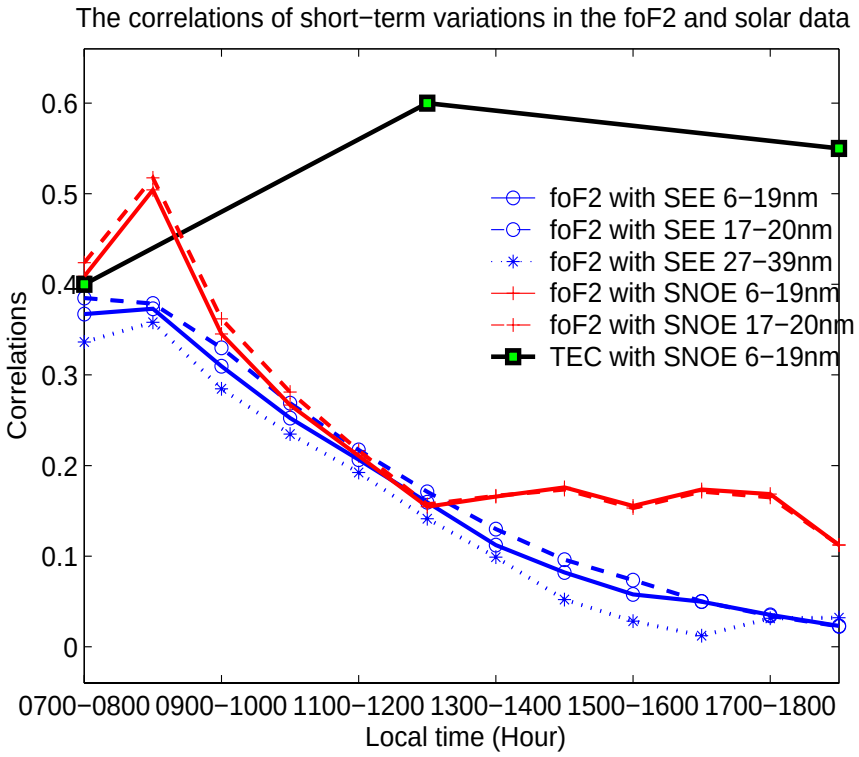

Figure 14. Correlations of short-term variations (27 day and less) of the daily solar irradiances and hourly foF2 data.

First, as shown in Figure 14, foF2 has slightly higher correlations with solar soft X-rays than with EUV. For example, the foF2 (0700-0800 LT) has a 0.38 correlation with the X-rays and a 0.33 correlation with the EUV. As shown in Figure 14, the average difference between the correlations, 0.05, is small but significant. To better understand this difference, we must first understand the relationship between the X-rays and EUV. If the X-ray and EUV irradiances were sufficiently correlated, both correlations would represent the same relationship with foF2. However, the 0.75-0.77 correlation between the X-rays (6-19 nm and 17-20 nm) and the EUV (27-39 nm) is lower than the 0.95 correlation between solar irradiances of 6-19 nm and 17-20 nm. Therefore, it is worth considering whether X-rays and EUV are redundant.

In order to understand the different relationships of foF2 with X-rays and EUV, the correlation of foF2 with each, separate from the effects of the other, should be examined. This is accomplished by calculating the partial correlations. The correlation between foF2 and X-rays (or EUV) that remain after controlling for the EUV (or X-rays) indicates whether the additional measurement of solar irradiance provides additional information about the dependence of foF2 on solar irradiance. Using foF2 at 0700-0800 LT and 0800-0900 LT as an example, the partial correlations between foF2 and X-rays (after isolating the EUV) are significant, 0.2 at 0700-0800 LT and 0.17 at 0800-0900 LT. Therefore, the soft X-rays and the EUV provide independent information that is useful for determining ionospheric densities.

While the soft X-rays are a better short-term indicator for foF2, the EUV is a better long-term indicator, as shown in Figure 15, which includes long-term (>27 days) changes. A correlation of 0.65, for example, is seen between EUV and foF2 at 0800-0900 LT, higher than the 0.55 correlation seen between X-rays and foF2. However, for all time scales both EUV and

X-rays show higher correlations (0.5 versus 0.35 in the short-term for example) with foF2 than F10.7 does. This is consistent with higher correlations seen between TEC and X-rays than those between TEC and F10.7 [*Wang et al.*, 2006].

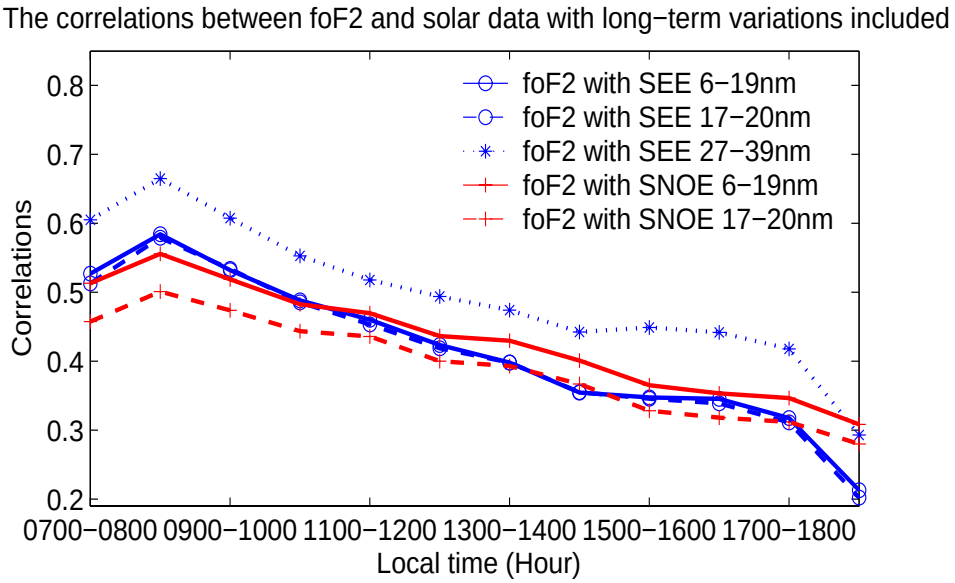

Figure 15. Correlations of variations between solar irradiances and foF2 when the long term (> 27 day) changes are included.

Second, as shown in Figure 14, correlations between foF2 and solar irradiances decrease from 0700 to 1900 LT. With both the EUV and the X-rays, correlations decrease from 0.4-0.5 in the morning to approximately 0.1 in the afternoon. Similar decreases are seen in measurements from either SNOE or TIMED. However, the correlations between X-rays (from the SNOE) and TEC (from Ancon, Peru) increase from morning to noon (from 0.4 to 0.6), and they do not change significantly from noon to afternoon (0.55), as shown in Figure 14. This indicates TEC and foF2 respond differently to the solar irradiance. The small correlations of foF2 with solar

irradiances in the afternoon (~0.1) suggest solar effects on short-term variations are insignificant, which is consistent with previous results [*Forbes et al.,* 2001; *Lastovicka et al.,* 2003; *Rishbeth and Mendillo,* 2001]; however, early in the morning there is a significant correlation.

Third, as shown in Figure 14, correlations in the afternoon are higher when using solar X-rays from SNOE (red dashed and solid lines) than those from TIMED (blue dashed and solid lines). The difference is distinct from 1400 to 1900 LT, when correlations between foF2 and X-rays are approximately twice as large for SNOE, as for TIMED (daily averages or individual orbits). The processing algorithms for both SNOE and TIMED data are similar [*Woods et al.,* 2005], but the data are from different time periods and from different parts of the solar cycle. The SNOE measurements used are from March 1998 to January 2000, the rising phase of the solar cycle with solar maximum in July 2000; and the TIMED measurements are from February 2002 to December 2004, the declining phase of the same solar cycle. Therefore, the difference between correlations in the afternoon may be due to either a random temporal variation or a variation with phase of the solar cycle.

4.4 Local Time Dependence of Temporal Variations in foF2

Other differences between foF2 observations in the morning and afternoon are seen in the short-term temporal variations. Power spectra (signal strength as a function of frequency) of the solar irradiances and foF2 at different times of the day are used to understand the temporal variations.

Representative examples of the power spectrum of foF2 are shown in Figures 16 and 17. In Figure 16 (a and b) the power spectra for two times in the morning, 0800-0900 LT and 1100-

1200 LT, are shown. In Figure 17 (a and b) two times in the afternoon, 1500-1600 LT and 1700-1800 LT, are shown. A ~ 27- day variation is seen in the early morning foF2 (Figure 4.5), the same time when a 0.4-0.5 correlation occurs between foF2 and solar irradiances. This indicates that the ~27-day variation is due to the solar irradiances, which is consisted with results from previous studies (for example, *Forbes et al*., [2001] and *Altadill et al*., [2003]).

At later times, near noon and in the afternoon, a shorter ~14 day period appears and the ~27 day period fades, as seen in Figures 16 (b) and 17. This variation seems to be related to variations in the solar wind and geomagnetic activity ([*Forbes et al*., 2001; *Mendillo et al*., 2002]). In order to better understand the effects of both solar irradiance and geomagnetic activity on the variation of foF2, the power spectrum of the solar EUV irradiances and ap, a 3-hour index of geomagnetic activity, is shown in Figure 18. A ~13.5 day variation is hardly above the average spectrum of solar EUV (Figure 18 a); however, a persistent ~13.5-day variation is seen in ap (Figure 18 b). It should be noted that the ~13.5-day variation is not always evident; it is discernable in less than half the measurements. The power spectrum results are consistent with the results from *Mursula and Zieger* [1996]. They found that the occurrence and persistence of the 13.5-day periodicity is more prominent in the solar wind and related geomagnetic activity indices than in solar fluxes during the maximum and declining phase of solar cycles. The observations used are from 2002 to 2004, also the declining phase of the solar cycle. Therefore, the ~14-day period in foF2 is attributed to geomagnetic activity. The ~14-day period is strongest in the afternoons, when the conductivity of the F region is largest.

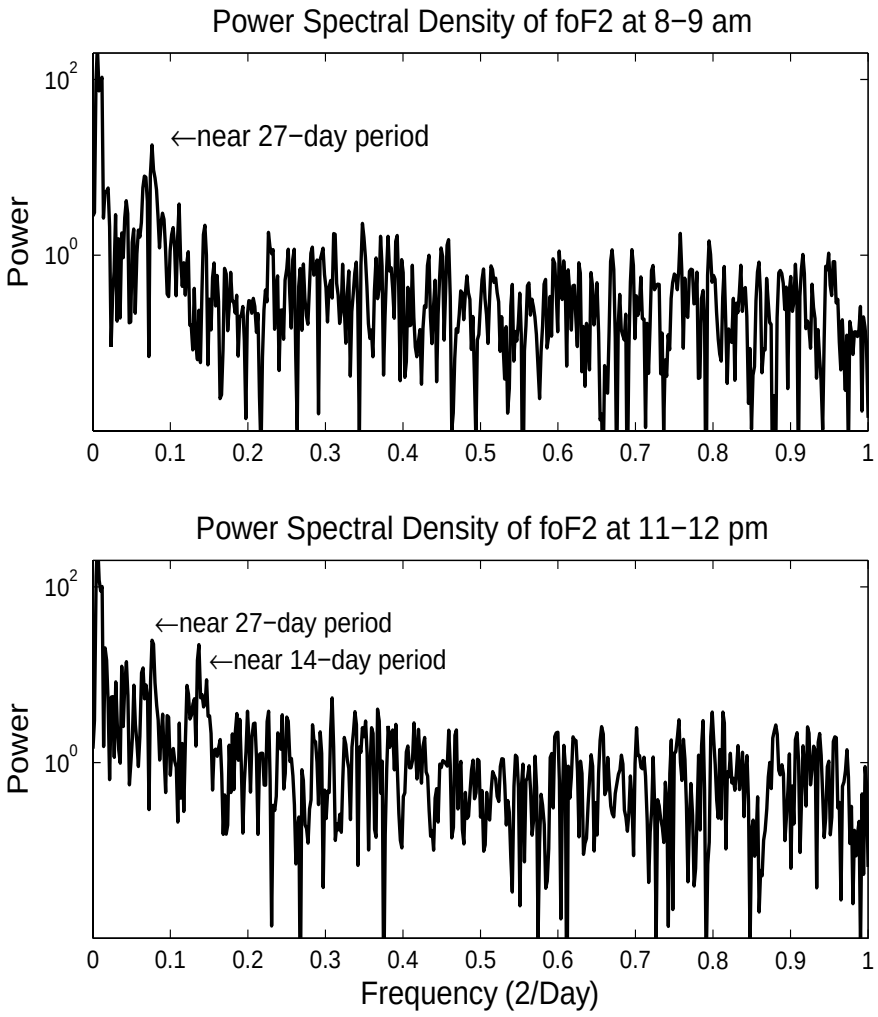

Figure 16. (a) Power spectral density of foF2 at 0800-0900 LT. (b) Power spectral density of foF2 at 1100-1200 LT.

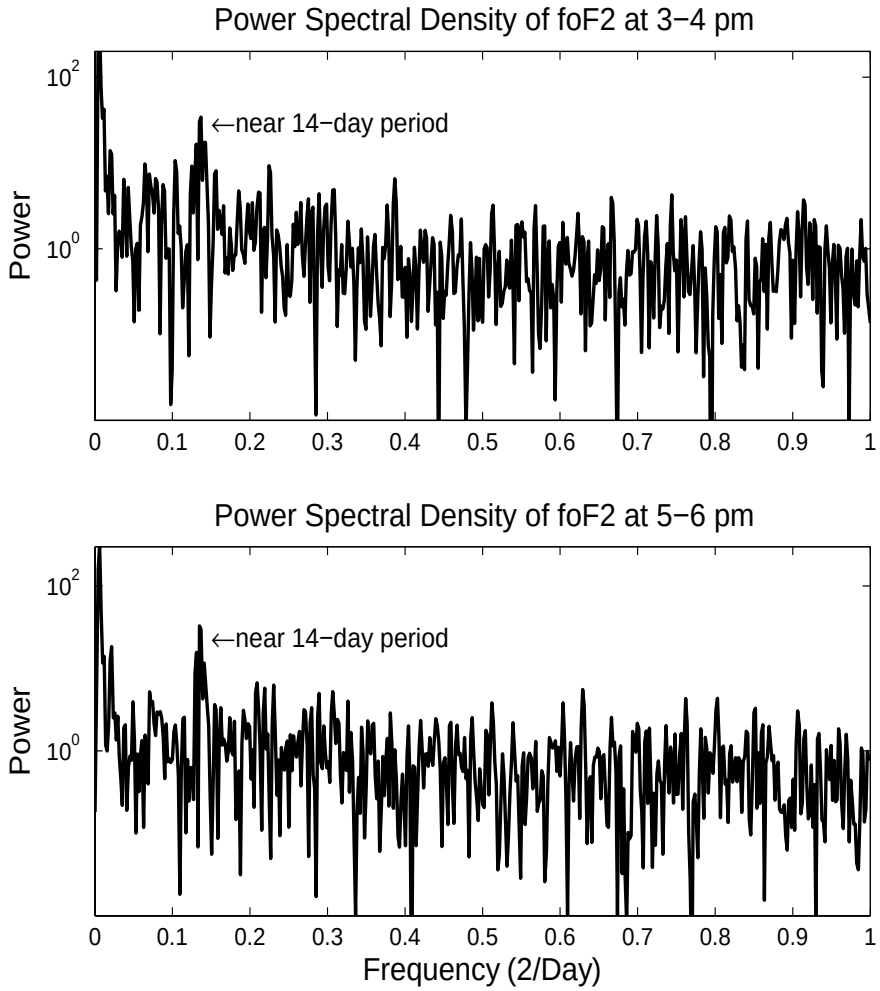

Figure 17. (a) Power spectral density of foF2 at 1500-1600 LT. (b) Power spectral density of foF2 at 1700-1800 LT. A ~14-day period is distinct throughout afternoon

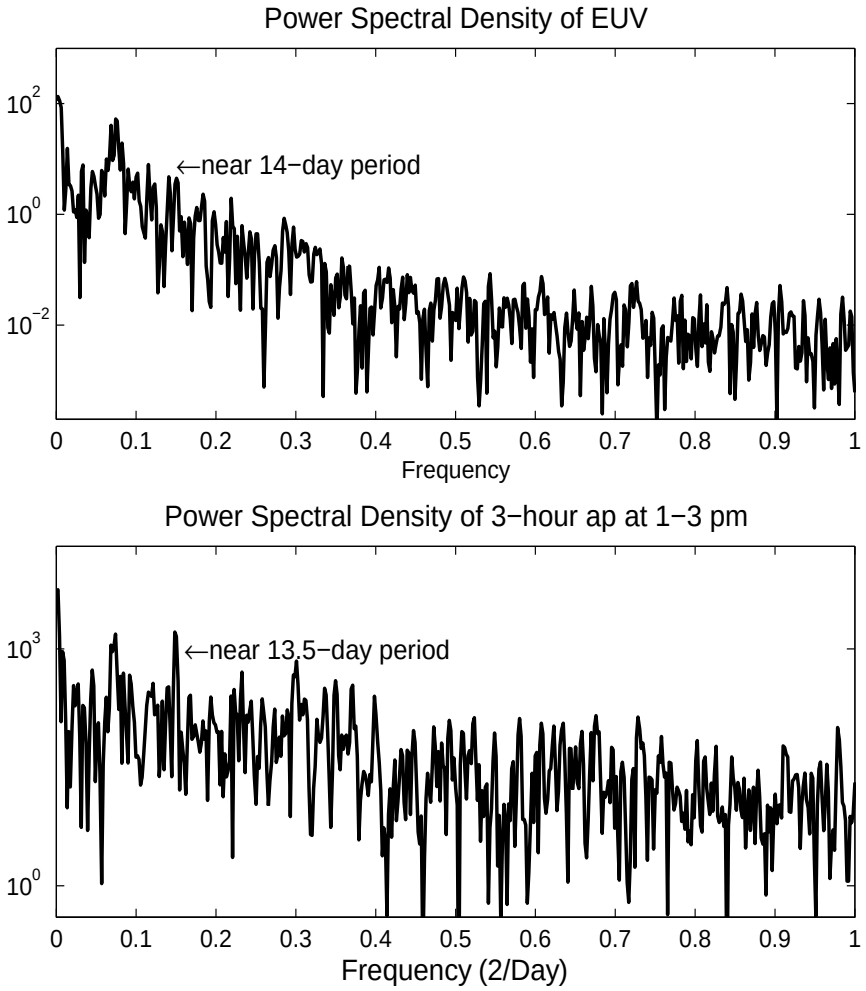

Figure 18. (a) Power spectral density of the 2002-2004 EUV measurements (27-39 nm) from TIMED. (b) Power spectral density of ap from 1300-1600 LT. A ~14-day period is distinct in the ap data, but not in the solar irradiance.

4.5 Summary

The short-term relationship of the equatorial peak electron density and the solar short wavelength irradiance was examined using foF2 observations from Jicamarca, Peru and solar

irradiance measurements from recent satellites using solar soft X-ray measurements from both the SNOE (1998-2000) and TIMED (2002-2004) satellites as well as extreme ultraviolet (EUV) measurements from the TIMED satellite. At short time scales (27 days or less) soft X-rays have a slightly larger correlation with foF2 than the EUV has; although, the EUV does show a higher correlation for longer periods. For the short-term (≤ 27 day) variations, both SNOE and TIMED observations have a higher correlation in the morning (~0.5) than the afternoon (~0.1). In the afternoon SNOE observations have a higher correlation (~0.2) with foF2 than the TIMED observations (~0.1 correlation). The difference in correlation may be due to either a random temporal variation or a variation with phase of the solar cycle. At morning times foF2 has a ~27 day variation, consistent with the solar rotation rate. After noon, but not in the morning, a ~14-day variation consistently appears in the foF2. This ~14 day variation is attributed to geomagnetic influences.

CHAPTER FIVE
IONOSPHERIC ELECTRON DENSITIES AND GEOMAGNETIC ACTIVITY

5.1 Introduction

The ionosphere plays an important role in Earth's space weather. As discussed in *Rishbeth and Mendillo* [2001], the day-to-day ionospheric variability is associated with strong coupling to regions below (e.g., through gravity and planetary waves) and above (e.g., through solar and geomagnetic activity). Consequently, understanding ionospheric density variations is a challenge. Recent studies have investigated the day-to-day variability of the ionosphere due to planetary wave activity [e.g., *Aburjania et al.,* 2003, 2004; *Altadill and Apostolov,* 2003; *Lastovicka et al.,* 2003; *Lastovicka and Sauli*, 1999; *Voiculescu and Ignat*, 2003; *Haldoupis et al.*, 2004]. The planetary waves in the F region showed variations with periods of 2, 5, 10, and 16 days at midlatitudes [*Lastovicka et al*. 2003]. At least 20–30% of the planetary waves with periods of about 2–3, 5–6 days were attributed to geomagnetic activity variations, as were 65–70% of the 10- and 16-day periods [*Altadill et al.,* 2003]. These studies suggest geomagnetic activity is an important factor in short-term variations of the ionosphere.

The effect of geomagnetic activity on the ionosphere has been examined during storm times in recent studies [e.g., *Buonsanto* et al. 1992 and 1993; *Richards et al.,* 1993; *Rishbeth,* 1991; *Field and Rishbeth,* 1997; *Basu et al.,* 2001; *Daniell and Strickland,* 2001; *Strickland et al.* 2001a, 2001b; *Fuller-Rowell et al.,* 2002]. In order to fully understand how the ionosphere varies in response to geomagnetic events, studies based on a wide range of conditions and over extensive time spans are needed. Since variations at periods of less than 10 days have been seen

in the ionosphere, geomagnetic activity and planetary waves [*Forbes et al.,* 2000; *Mendillo et al.,* 2001; *Altadill et al.,* 2003; *Lastovicka et al*. 2003], by examining these periods, a more detailed understanding of the relationship between the ionosphere and geomagnetic activity may be obtained.

The critical frequency of the F2-layer (foF2) is a measure of ionospheric peak electron density in the F2 region [*Rishbeth et al*., 2001; *Forbes et al.,* 2000; *Mendillo et al.,* 2002; *Altadill et al.,* 2003]. The Total Electron Content (TEC) measures the integrated electron densities from the D, E, F and topside regions [*Pi et al.*, 1997; *Kelly et al.,* 1996; *Lunt et al.,* 1999 a and b; *Valladares et al.,* 2001; *Kutiev et al.,* 2005]. This dissertation examines the dependence of both TEC and foF2 measurements on Dst, an indicator of equatorial geomagnetic activity.

Wavelets can be used to decompose a signal into components with the desired frequency resolution [*Mallat et al.,* 1989]. While recent studies have applied wavelet methods to space physics, most have used conventional 2-channel wavelets available in commercial software such as MATLAB [e.g. *Fagundes et al.,* 2005; *Grinsted et al.,* 2004; *Pancheva et al.,* 2000 and 2004]. For this study a detailed understanding of variations with periods $\leq$ 10 days are expected. A 3-channel wavelet, which is used in the following analysis, can provide more insights to the periodicities since it can represent more frequency components than the conventional 2-channel.

This chapter discusses: (1) the wavelet filters and 3-channel filter banks; (2) wavelet performance testing; (3) data description; (4) data analysis and results; (5) discussion; (6) conclusions.

5.2 Wavelet Filters and Filter Banks

5.2.1 Wavelet Filters

Many observations (*e.g.*, from the ionosphere) are recorded in the time domain, with both the averages and differences having importance. The averages can represent the long-term variations of signals, and the differences can represent the variations over a short time period. Both can be represented using Harr wavelets (seen in Chapter 2). They are simple and therefore easier to use than more complex wavelets. For this reason they are used in the following analysis.

A key to using wavelet methods is to properly define the filters. Detailed filter design algorithms were given by *Strang* [1996], and several conditions considered in this study are: (1) wavelet definition as shown in Equation 2.18 and 2.19; (2) orthogonality of wavelet filters; (3) the lossless principle which guarantees perfect reconstruction from filter banks (see Appendix B); (4) realization of averaging and differencing; (5) detailed representation of periodicities ≤ 10 days. The scaling and wavelet filters used are:

Scaling filter: $H_0 = [1 \;\; 1 \;\; 1]$

Wavelet filter 1: $H_1 = [-\frac{\sqrt{2}}{2} \;\; \sqrt{2} \;\; -\frac{\sqrt{2}}{2}]$

Wavelet filter 2: $H_2 = [\frac{\sqrt{6}}{2} \;\; 0 \;\; -\frac{\sqrt{6}}{2}]$

5.2.2 Filter Banks

Wavelet transforms of the data are implemented using the scaling and wavelet filters (above) as 3-channel filter banks. As shown in Figure 19, 3-channel filter banks consist of analysis banks, synthesis banks, down-samplers and up-samplers. The analysis banks consist of a scaling filter H_0 and two wavelet filters H_1 and H_2, which partition the spectra of an input signal into three bands. The synthesis banks, as shown in Figure 19, consist of synthesis filters which are time inverse of the analysis filters. While analysis filters split an input signal, synthesis filters recombine it. The outputs of the down-samplers are wavelet coefficients and scaling coefficients; the outputs of the synthesis banks are reconstructed components at each resolution. Since the reconstructed components are directly related to the coefficients through linear filters and up-samplers, they share the same characteristics. The wavelet coefficients, rather than the original signals, are used in the subsequent analysis.

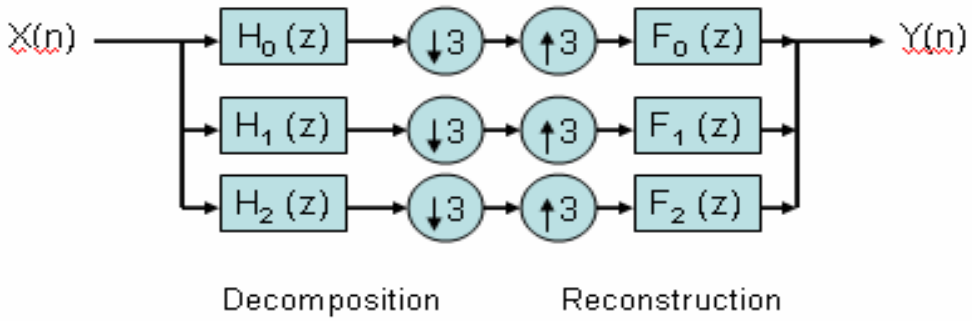

Figure 19. 3-channel filter banks with one level.

The analysis presented here uses filter banks with three levels, as shown in Figure 20. The wavelet coefficients from the first level represent variations with periods near 3 days; those

from the second level represent variations with periods near 9 days; similarly, the third level is for near 27-day variations. As shown in Figure 20, the first two levels produce a total of four sets of wavelet coefficients which represent variations with periods near 3 and 9 days. Compared to conventional 2-channel wavelets with three sets (i.e., scale 2, 4 and 8), the 3-channel methods can represent more details of an input signal with periods ≤ 10.

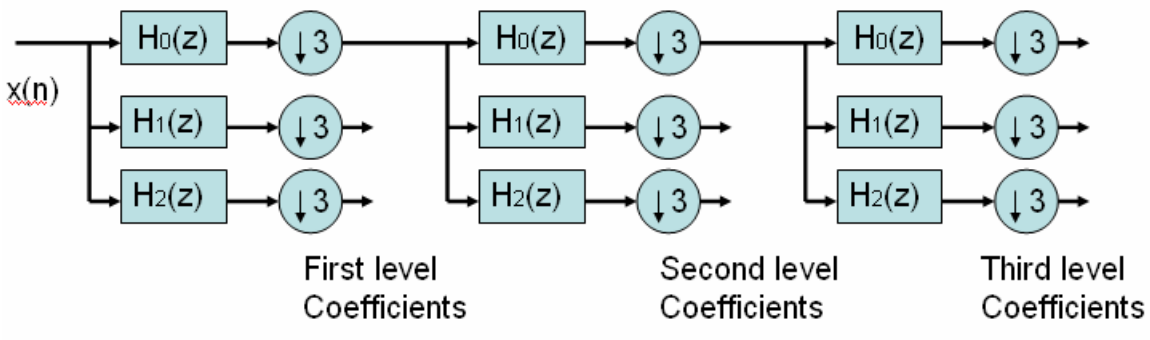

Figure 20. 3-channel filter banks with 3 levels (only the analysis banks are shown).

5.3 Testing

Tests of the wavelet filters help us understand their ability to represent short-term variations in the data.

5.3.1 Wavelet Filter Performance Testing

Test signals, with periods of 2 to 27 days, were input to the filter banks. Though periods of 2-10 days are of interest, the testing signals are expanded to 27-day periods in order to better understand which frequencies each filter extracts.

In order to determine the effect of each filter, the wavelet coefficients from each filter at each level are examined using Welch's power spectrum analysis method. The powers change as the testing signals vary. All testing signals, as well as the powers of the coefficients, are normalized in order to better understand the filters. The normalized power extracted by each filter is shown in Figure 21 for input periods varying from 2 to 27 days. Only the results from the first two levels are shown, which represent variations near or less than 10 days.

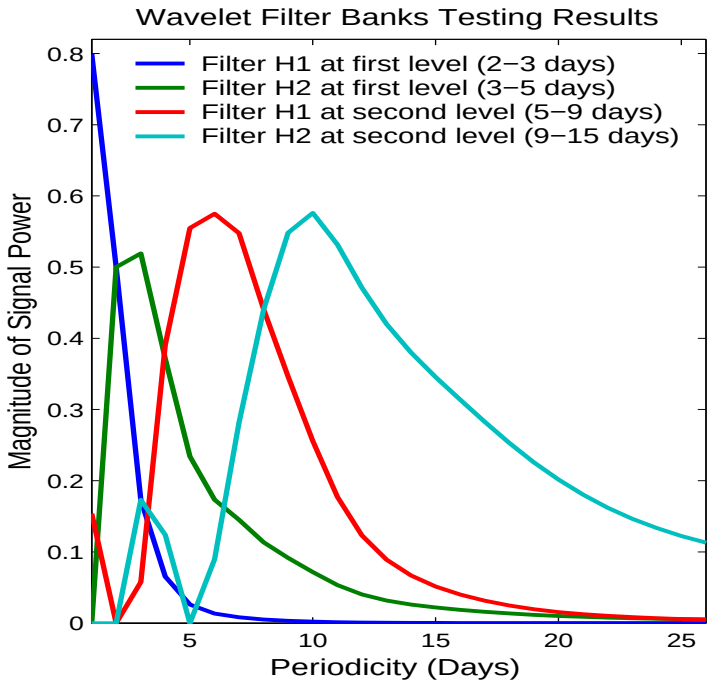

Figure 21. Frequency response of the wavelet filters

5.3.2 Testing Results Analysis

As shown in Figure 21, the wavelet filters can best extract the short-term variations with periods of 2-3, 3-5, 5-9 and 9-15 days. For example, H_1 filter at the first level can extract most of the 2-3 day variations (0.5-0.8), and at the second level it extracts 0.4-0.6 of the 5-9 day variations. Therefore, the filters can be used to study the short-term variations at these scales.

Wavelet filters have some disadvantages. First, the longer-term variations may affect the performance. The filter H_2 at Level 9, which is expected to extract the 9-15 day periodicities, also represents 0.16-0.34 of the16-23 day signal. Second, period overlaps are seen between wavelet filters. The 6-7 day periodicity for example, which is mostly represented by filter H_1 at the second level, can also be partly represented (0.17-0.23) by filter H_2 at the first level. Therefore, given an input signal with mixed periods from 2 to 23 days, the desired performance of wavelet filters would be affected.

5.3.3 Improvement Methods

In order to improve the performance of the wavelet filters, the unneeded variations (*e.g.,* long-term variations) should be removed before application of the filter banks. This can be realized by using a Fourier transform as a preprocessor. A Fourier transform breaks a time series, x, into constituent sinusoids of different frequencies, as is displayed in Equation (5.1). By setting the part of the Fourier transform x_i which corresponds to the unneeded frequency band to 0 and leaving the other parts unchanged, then applying an inverse Fourier transform (Equation

5.2) produces a transformed signal with the unneeded frequencies removed.

$$X(k) = \frac{1}{N}\sum x(n)e^{-j2\pi(k-1)(\frac{n-1}{N})} \qquad 1 \le k \le N \tag{5.1}$$

$$x(j) = (1/N)\sum_{k=1}^{N} X(k)\varpi^{-(j-1)(k-1)} \tag{5.2}$$

where $\varpi_N = e^{(-2\pi i)/N}$.

A combination of a random noise signal and four periodic variations (9-day, 13-day, 27-day, 36-day) are used to test this algorithm. The goal is to remove periods ≥ 27 days and preserve the other periods. The power spectra of the test signals are calculated before and after applying this algorithm. As shown in Figure 22 (a) and (b), the longer periods are removed as desired. In the following analysis this method is used to preserve periods $\leq$ 11 days.

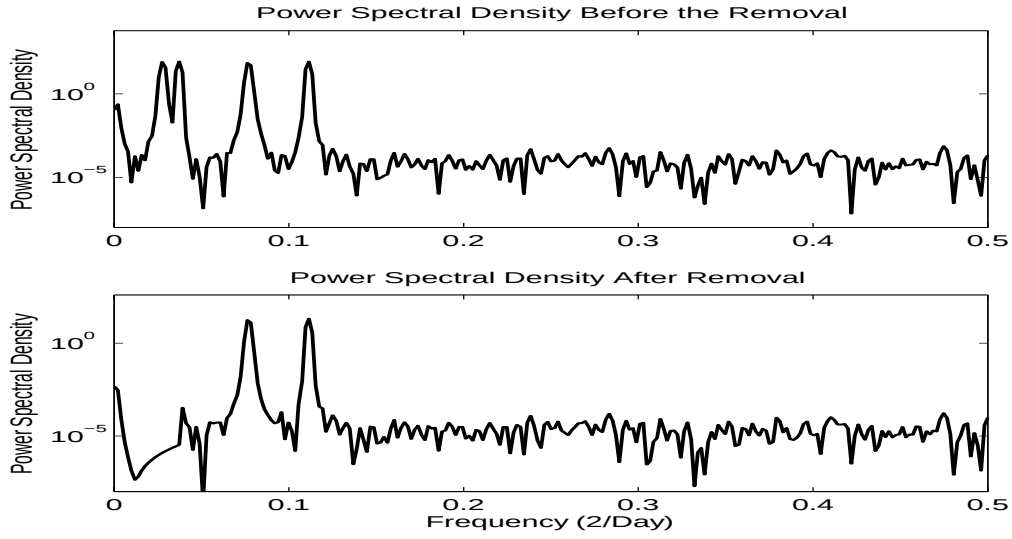

Figure 22. Power spectrum of a test signal before and after removing the 27- and 36-day variations using the Fourier transform method

5.4 Data

Two measures of the ionosphere, TEC and foF2, are examined in this study. The TEC is the integrated electron density in the ionosphere. As discussed in Chapter 2, a GPS receiver located near Ancon, Peru (-77.15° longitude, -11.78° latitude, 1.47 degrees geomagnetic latitude) provides the TEC measurements for this study [*Valladares et al.,* 2001]. Observations from 11 March 1998 to 23 August 1999 are used here. For these dates the average TEC measurement was calculated for all observations whose ionospheric pierce point occurred within -12 ± 2 degrees latitude and -77 ± 2 degrees longitude and within the hour selected. The measurements from three local hours, 0700-0800 LT, 1200-1300 LT and 1700-1800 LT, are collected.

The foF2 data are from a digisonde at Jicamarca Radio Observatory in Peru [*Reinisch et al.,* 1996], and detailed descriptions of the data are given in Chapter 4. The hourly averages foF2 data at 0700-0800 LT, 1200-1300 LT and 1700-1800 LT are used from March 1998 to August 1999. An example of TEC and foF2 data, collected from 1200-1300 LT, is shown in Figure 24 (a and b).

Dst, which is derived from magnetometer measurements at low latitudes, is used to represent geomagnetic activity. Hourly Dst data are available online through the website http://ftp.ngdc.noaa.gov/STP/GEOMAGNETIC DATA/INDICES/DST/. An example of Dst data at 1200-1300 LT is shown in Figure 25. Generally, values of -50 nT or less are indicative of a storm-level disturbance, and values of -200 nT or less are associated with middle-latitude auroras.

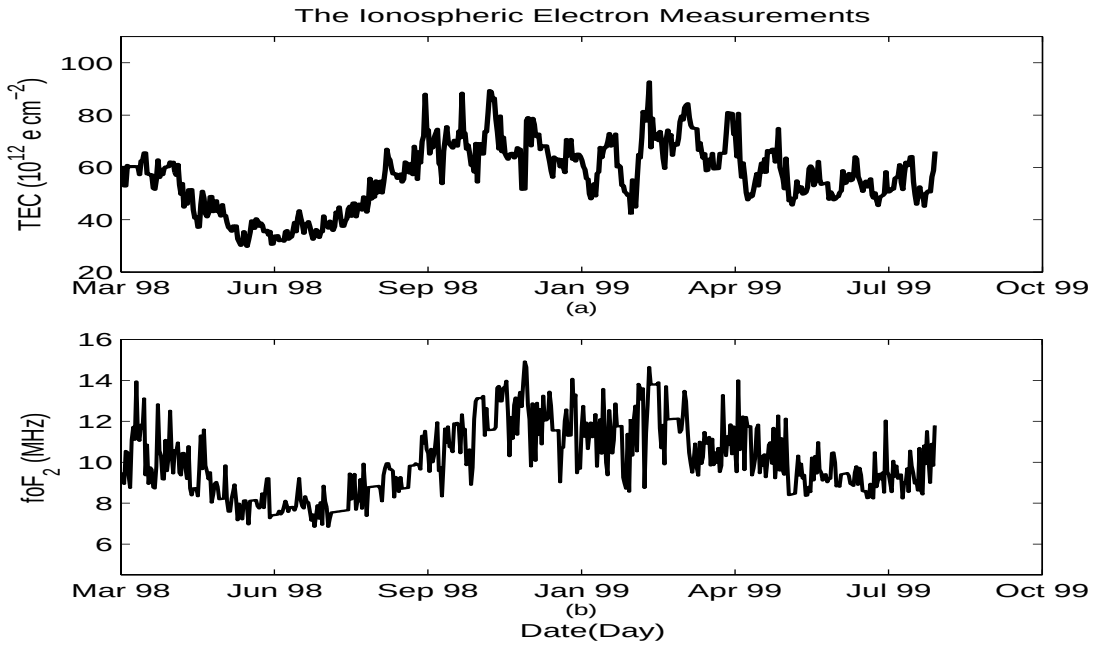

Figure 23. TEC and foF2 data at 1200-1300 LT from 1998 to 1999. (a) The TEC is from a GPS receiver in Ancon, Peru; (b) The foF2 is from a digisonde in Jicamarca, Peru.

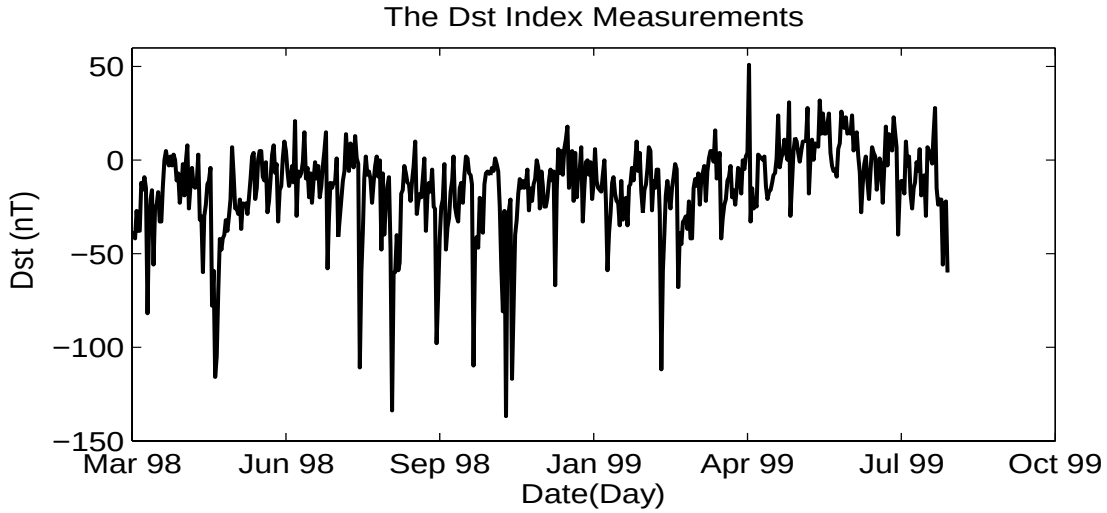

Figure 24. Dst measurements from 1998 to 1999.

5.5 Data Analysis and Results

The TEC, foF2 and Dst data are compared next. Since these data contain both short-term and long-term components, they are preprocessed using a Fourier transform and the residuals are then decomposed using wavelet filters. As discussed earlier, the resulting wavelet coefficients represent variations with periods of 2-3, 3-5, 5-9 and 9-11 days respectively. Cross-correlations between the ionospheric and Dst data are then examined using the coefficients at each scale. This analysis procedure is shown in Figure 25. The preprocessor can remove both long-term variations and period overlaps; however, no significant difference was seen in their correlations from those by removing long-term variations. The latter are used in the following discussion.

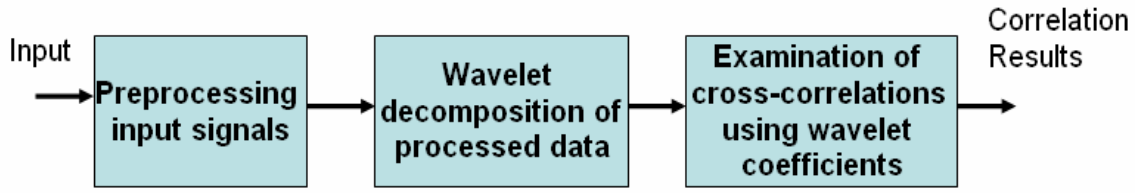

Figure 25. Flow chart of signal processing using wavelet methods.

5.5.1 TEC and Dst Comparison

Shown in Figure 26 are the correlations between TEC and Dst at each of the four time scales at 0700-0800 LT, 1200-1300 LT and 1700-1800 LT respectively. While the correlations between the ionosphere and Dst are negative, due to Dst being negative, the magnitudes of

correlations at each scale are used here. There are significant correlations between TEC and Dst. The correlations range from 0.25 to 0.53 at scale of 2-3 days, 0.25 to 0.51 at 3-5-days, 0.3 to 0.55 at 5-9 days, and 0.3 to 0.47 at 9-11 days. The average of these correlations is as high as ~0.4. These correlations suggest a significant relationship between ionospheric variations and geomagnetic activity at these short-term scales. While recent studies suggested that the geomagnetic activity may drive 0.2-0.3 of planetary waves at scales of 2-3, 5-6 and 10 days [*Altadill et al.,* 2003; *Fagundes et al.,* 2005], the direct comparison of the Dst and TEC shows more significant correlations (~0.4).

As seen in Figure 26 the correlations between the Dst and TEC increase from morning to afternoon. The increase is seen at all scales: 2-3, 3-5, 5-9 and 9-11 days. For example, at scales of 2-3 days, the correlation increases from 0.25 (in the morning) to 0.43 (at noon) and 0.53 (in the afternoon). The F region conductivity also increases throughout the daytime, and this similarity raises a possible connection between TEC and F region conductivity.

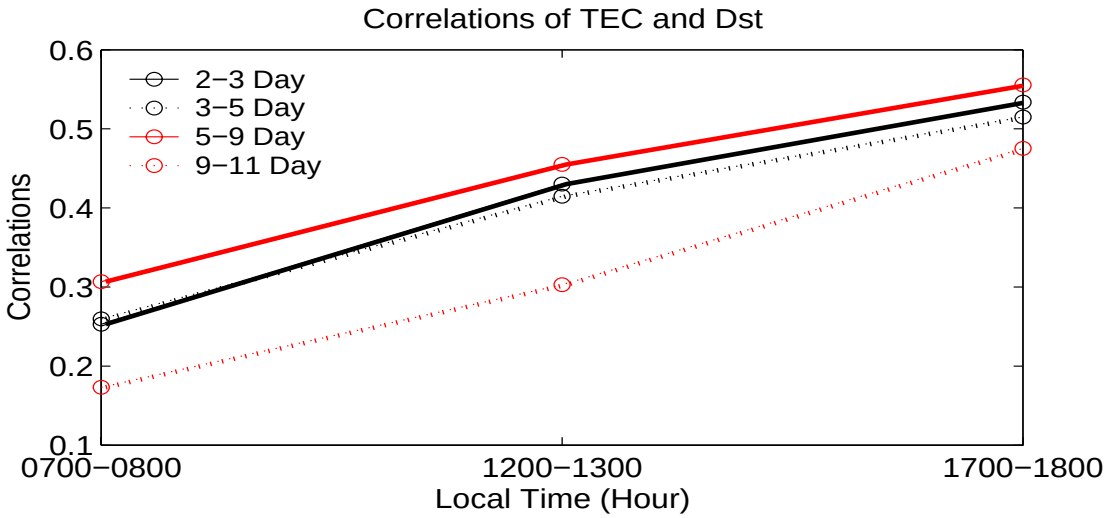

Figure 26. Correlations between Dst and TEC at Ancon, Peru as a function of local time.

5.5.2 foF2 and Dst

The correlations of foF2 with Dst, as shown in Figure 27, are smaller than for TEC. Their variation with local time is also different. On average the correlations are over 0.2 lower for foF2 than for TEC. While the foF2 represents peak electron densities at the F2 layer, the TEC is integrated electrons densities from the D, E, F (F1 and F2) and topside layers of atmosphere. Since the foF2 is more sensitive than the TEC to couplings from below and above, this might explain the different correlations of foF2 and TEC with the Dst.

5.6. Discussion

Geomagnetic activity is often divided into quiet times, moderately disturbed times and storms. While most recent work have focused on storm times (Dst < -50), the ionospheric response to geomagnetic activity in the quiet/moderate conditions (Dst > -50) has significant importance for forecasting the space weather. In order to understand the effects of quiet/moderate geomagnetic activity, the TEC and Dst data are examined when Dst >-50. Observations from 1200-1300 LT are used here. The correlations between TEC and Dst are shown in Table 2. As a comparison, those only using quiet time data, as well as using the original data (including all geomagnetic conditions), are also presented in Table 2.

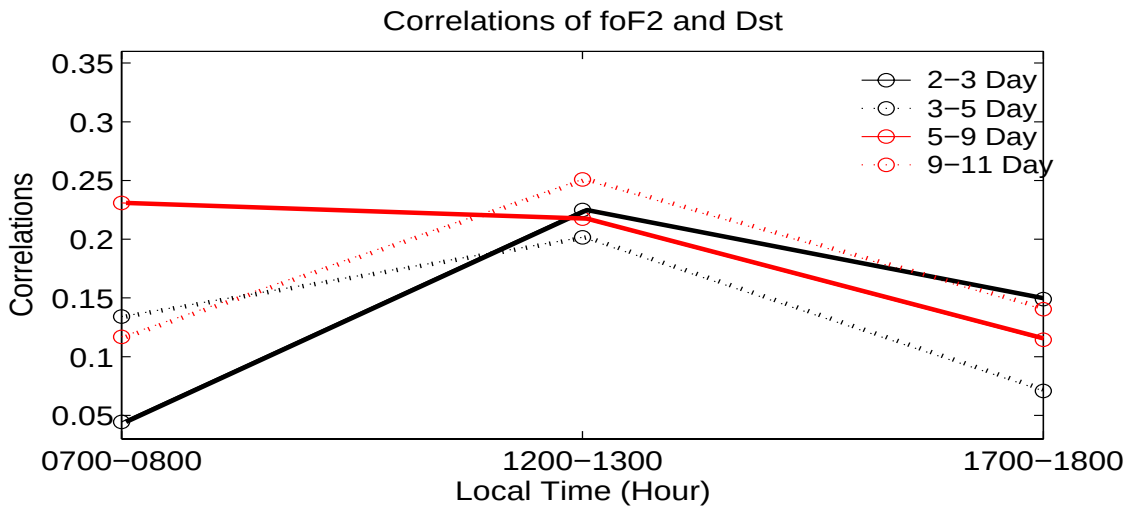

Figure 27. Correlations between Dst and foF2 and at Jicamarca, Peru as a function of local time.

The correlation between TEC and geomagnetic activity increases with geomagnetic activity as shown in Table 2. During quiet times the correlations are small ($\leq$ 0.2), but more distinct correlations (~0.3) are seen when the geomagnetic activity is moderate/quiet. A correlation of 0.37 is seen at the 2-3 day scale and a 0.3 correlation is seen at both 3-5 and 5-9 day scales when Dst > -50. These correlations suggest the importance of moderate/quiet geomagnetic events on short-term ionospheric variations. At longer time scales the correlations decrease, which is consistent with geomagnetic activity having less effect on the longer-term ionospheric variations.

Table 2. Cross correlations between TEC and Dst at noon time under different geomagnetic conditions

	Dst>-20	Dst >-50	Dst all
2-3 day	-0.21545	-0.36864	-0.43005
3-5 day	-0.15581	-0.30953	-0.41464
5-9 day	-0.14066	-0.30759	-0.45501
9-12 day	-0.16629	-0.19556	-0.30294

5.7 Conclusions

The short-term relationship between equatorial ionosphere and geomagnetic activity is examined. Hourly averages of the Total Electron Content (TEC) and critical frequency of the F2 layer (foF2) are compared with the hourly measurements of Dst, a proxy for the equatorial geomagnetic activity, at three local times (0700-0800 LT, 1200-1300 LT and 1700-1800 LT) from 1998 to 1999. These data are analyzed with a 3-channel wavelet transform which can well represent variations with periodicity of 2-3, 3-5, 5-9 and 9-11 days. At these time scales, significant correlations (~ 0.4) are seen between TEC and Dst, with correlations increasing from morning to afternoon. Correlations between foF2 and Dst (~0.2 at local noon) are smaller and they peak at local noon, rather than increasing throughout the daytime hours. When geomagnetic activity is moderate-quiet (Dst > -50), a distinct correlation (~ 0.3) is seen between TEC and Dst in those short-term scales.

CHAPTER SIX
SUMMARY

The Earth's daytime ionosphere is strongly coupled to external influences. It is coupled to the Sun, through solar irradiance and geomagnetic activity, and to lower altitudes by tides and atmospheric waves. This dissertation examines - in the first study using long-term, daily observations - how the low latitude ionosphere depends on the Sun's short wavelength irradiance and the Earth's geomagnetic activity.

Extreme ultraviolet (EUV) and soft X-ray emissions from the Sun produce most of the ionosphere. Due to a lack of EUV and soft X-ray measurements, proxies like the Sun's 10.7 cm radio flux (F10.7), have been used as a substitute in most previous research. This dissertation uses direct measurements of the short wavelength solar irradiances to improve our understanding of the short-term relationship between solar irradiance and the ionosphere. The Sun also produces the solar wind, which is responsible for geomagnetic activity. This geomagnetic activity plays an important role in ionospheric variations, and its effects are also examined.

Data from several instruments is used. Solar soft X-ray measurements from both the SNOE and TIMED satellites are used, as are solar EUV measurements from the TIMED satellite. To represent the geomagnetic activity in the equatorial region, Dst is used. Ionospheric data - TEC from a GPS receiver in Ancon, Peru and foF2 from a digisonde in Jicamarca, Peru – are compared with the solar and geomagnetic data.

Various signal processing techniques are used. Classical time series analysis is used to analyze data from the time domain, and digital signal processing methods are applied to

understand data from the frequency domain. In addition wavelet methods, capable of combining both the time and frequency domain analysis, are also used.

6.1 Conclusions

Significant correlations are seen between TEC and short wavelength solar irradiances at both ~27-day and shorter-term time scales. Solar irradiances from the previous 2-3 days have a distinct correlation (0.3) with the present day's TEC, and the delays are consistent with neutral densities affecting the ionosphere. These correlations are significantly higher than those seen between F10.7 and TEC. This is the first time solar irradiance effects on the ionosphere have been identified at such large time delays.

Higher correlations are seen between foF2 and soft X-rays than between foF2 and EUV for time scales of $\leq$ 27days. Since solar EUV radiation produces most of the ions in the F region, a higher correlation with the soft X-rays is not expected. Both the EUV and soft X-rays have a higher correlation with the foF2 than F10.7 does.

The solar-ionosphere correlations also vary with local time. Correlations between TEC and solar irradiance increase from morning to afternoon. The opposite behavior is seen for foF2 and solar irradiance, where correlations decrease significantly from morning to afternoon. The TEC has higher correlations than foF2 with solar irradiance.

In comparisons of the ionosphere and geomagnetic activity, detailed correlations were obtained at scales of 2-3, 3-5, 5-9 and 9-11 days. At these scales significant correlations (~0.4) are seen between TEC and Dst, suggesting geomagnetic activity has a significant effect on short-

term variations. The correlations between TEC and Dst increase from the morning to the afternoon (0.2 to 0.5). While they are less dramatic than the changes seen during geomagnetic storms, distinct correlations (0.3) are seen between the TEC and moderate/quiet geomagnetic activity at these short-term scales.

6.2 Future Research

The results indicate several interesting possibilities for further research:

(1) Neutral atmosphere

Including neutral atmosphere data would provide a better understanding of the relationship between neutral and electron densities. The 1-3 day phase difference between solar irradiance and TEC is similar to the phase difference between solar irradiance and neutral density, but several possibilities exist. These include the ratio of O and N_2, Nitric oxide densities, neutral temperatures and neutral winds. There are suitable data available for studying each.

(2) E region density

The E region may have an effect on the F region, due to the sensitivity of F-region densities to changes in height and the soft X-rays changing E-region conductivities. Comparison of E-region densities with changes in the F-region would allow E-region effects to be identified.

(3) Modeling studies

Model calculations, by The Thermosphere Ionosphere Electrodynamics General Circulation Model (TIEGCM) for example, can provide insight into the possible physical mechanisms responsible for the correlations, and therefore provide a means of testing our understanding.

(4) Techniques

A variety of statistical time series and digital signal processing techniques have been used in this dissertation. These techniques enable one to (1) understand the temporal and frequency variations of the data; (2) extract the autocorrelations from the signals using filters so that accurate cross-correlations may be obtained between signals; (3) define the phase delays; and (4) find the best fit model to represent input-output relationship. These techniques will continue to be used in future research. Combining the wavelet methods with adaptive signal processing techniques will be explored to provide a better understanding of how the ionosphere depends on solar irradiance and geomagnetic activity.

APPENDIX A: BIVARIATE NORMAL THEOREM

Theorem 2.1:

Let $\{X_t\}$ be a bivariate time series whose components are defined by

$$X_{t1} = \sum_{k=-\infty}^{\infty} \alpha_k Z_{t-k,1}, \qquad \{Z_{t1}\} \sim IID(0, \sigma_1^2),$$

$$X_{t2} = \sum_{k=-\infty}^{\infty} \beta_k Z_{t-k,2}, \qquad \{Z_{t2}\} \sim IID(0, \sigma_2^2),$$

where the two sequences $\{Z_{t1}\}, \{Z_{t2}\}$ are independent, $\sum_{k=-\infty}^{\infty} |\alpha_k| < \infty$ and $\sum_{k=-\infty}^{\infty} |\beta_k| < \infty$.

Then for all integers h and k with $h \neq k$, the random variables $n^{\frac{1}{2}} \rho_{12}(h)$ and $n^{\frac{1}{2}} \rho_{12}(k)$ are approximately bivariate normal with mean 0, variance $\sum_{j=-\infty}^{\infty} \rho_{11}(j)\rho_{22}(j)$, and covariance $\sum_{j=-\infty}^{\infty} \rho_{11}(j)\rho_{22}(j+k-h)$, for n large.

APPENDIX B: LOSSLESS SYSTEM

Definition 5.1:

Let $H(z)$ be a $p \times r$ system. $H(z)$ is said to be lossless if (a) each entry $[H(z)]_{km}$ is stable and (b) $H(z)$ is unitary on the unit circle, that is,

$$H^{H}(e^{jw})H(e^{jw}) = cI_r$$

for all $w \in [0,2\pi)$, and some real constant c. If c=1, then $H(z)$ is known as a normalized lossless system.

REFERENCES

Afraimovich, E. L., A. T. Altyntsev, E. A. Kosogorov, N. S. Larina, and L. A. Leonovich, (2001), Ionospheric effects of the solar flares of September 23, 1998 and July 29, 1999 as deduced from global GPS network data, *J. Atmos. Sol. Terr. Phys., 63*(17), 1841–1849

Altadill, D. and E. M. Apostolov, (2003), Time and scale size of planetary wave signatures in the ionospheric F region: Role of the geomagnetic activity and mesosphere/lower thermosphere winds, *J. Geophys. Res., 110* (A01312), doi:10.1029

Anderson, T. W., (1971), *The statistical analysis of time series*, John Wiley, New York

Aoki, M., (1987), *State space modeling of time series*, Springer-Verlag, Berlin

Appleton, E. V. and L. J. Ingram., (1935), Magnetic storms and upper atmosphere ionization, *Nature, 136,* 548-549

Bailey, S. M, T. N. Woods, C. A. Barth, and S. C. Solomon, R. Korde, L. R., Canfield., (2000), Measurements of the solar soft X-ray irradiance by the Student Nitric Oxide Explorer: first analysis and underflight calibrations, *J. Geophys. Res., 105*(A12), 27179

Bailey, S. M., T. N. Woods, F. G. Eparvier, and S. C. Solomon, (2005), Observations of The solar soft X-ray irradiance by the Student Nitric Oxide Explorer, *Adv. Space. Res., 37, (2), 209-218*

Bailey, S. M., T. N. Woods, C. A. Barth, and S. C. Solomon, (1999), Measurements of the Solar Soft X-ray Irradiance from the Student Nitric Oxide Explorer, *Geophys. Res. Lett., 26* (9), 1255-1258

Balan, N., G. J. Bailey, B. Jenkins B, P. B. Rao, R. J. Moffett, (1994), Variations of ionospheric ionization and related solar irradiances during an intense solar cycle, *J. Geophys. Res., 99* (A2), 2243-2253

Basu, S., Su Basu, K. M. Groves, H.-C. Yeh, S.- Y. Su, F. J. Rich, P. G. Sultan and M. J. Keskinen, (2001), Response of the equatorial ionosphere in the South Atlantic region to the great magnetic storm of July 15, 2000, *Geophys. Res. Lett., 28 (18),* 3577-3580

Bloomfield, P., (2000), *Fourier analysis of time series: An introduction*, 2nd edition, John Wiley, New York

Box, G. E. P. and G. M. Jenkins, (1976), *Time series analysis: Forecasting and Control,* Revised Edition, Holden-day, San Francisco

Brockwell, P. J. and R. A. Davis, (1991), *Time series: theory and methods*, 2nd edition, Springer-Verlag, New York

Brockwell P. J. and R A. Davis, (1996), *Introduction to Time Series and Forecasting,* Springer, New York

Buonsanto, M. J., J. C. Foster, and D. P. Sipler, (1992), Observations from Millstone Hill during the geomagnetic disturbances of March and April 1990, *J. Geophys. Res., 97*, 1225

Buonsanto, M. J., J. C. Foster, (1993), Effects of magnetospheric electric fields and neutral winds on the low-middle latitude ionosphere during the March 20-21 1990 storm, *J. Geophys. Res., 98,* 19, 133

Burg, J. P., (1968), A new analysis technique for time series data, NATO advanced study institute on signal processing with emphasis on underwater acoustics, August 12-23. Reprinted in *Modern spectrum analysis*, IEEE press, New York

Chan, Y.T., (1992), *An introduction to wavelets,* Kluwer Academic Publishers, Boston

Daubechies, I., 1988, Orthonormal bases of compactly supported wavelets*, Comm. Pure Appl. Math., 41,* 909-996

Davies, K., (1980), Recent progress in satellite radio beacon studies with particular emphasis on the ATS-6 radio beacon experiment, *Space Sci. Rev., 25,*357

Duhamel, P. and M. Vetterli, Fast Fourier Transforms: A Tutorial Review and a State of the Art, *Signal Processing, 19*, April 1990, 259-299

Eastes, R., S. Bailey, F. Marcos, J. Wise, and T. Woods, (2004), The correspondence between thermospheric neutral densities and broadband measurements of the total solar soft X-ray flux, *Geophys. Res. Lett., 31,* 19804, doi: 10.1029 /2004GL020801.

Esteban, D. and C. Galand, (1997), Application of quadrature mirror filters to split band coding, *IEEE ICASSP*, Hartfort

Evans, J. V., (1977), Satellite beacon contributions to studies of the structure of the ionosphere, *Rev. Geophys., 15,* 325.

Fagundes, P. R., V. G. Pillat, M. J. A. Bolzan, Y. Sahai, F. Becker-Guedes, J. R. Abalde, and S. L. Aranha, (2005), Observations of F layer electron density profiles modulated by planetary wave type oscillations in the equatorial ionospheric anomaly region, *J. Geophys. Res, 110* (A12302), doi:10.1029

Field, P. R. and H. Rishbeth, (1997), The response of the ionospheric F2-layer to geomagnetic activity: an analysis of worldwide data, *J. Atmos. Sol. Terr. Phys., 59 (2),* 163-180

Forbes, J.M., S.E. Palo, X. Zhang, (2000), Variability of the ionosphere, *J. Atmos. Sol. Terr. Phys., 62,* 685–693

Fuller-Rowell, T. J., M. V. Codrescu, R. J., Moffett and S. Quegan, (1994), Response of the thermosphere and ionosphere to geomagnetic storms, *J. Geophys. Res., 101*, 2343-2353

Fuller-Rowell, T. J., (1997), The "thermospheric spoon": A mechanism for the semiannual density variation, *J. Geophys. Res.*, *103* (A3), 3951-3956

Fuller-Rowell, T. J., G. H., Millward, A. D. Richmond, M.V. Codrescu, (2002), Storm-time changes in the upper atmosphere at low latitudes, *J. Atmos. Sol. Terr. Phys., 64,* 1383-1391

Grinsted, A., J. C. Morre and S. Jevrejeva, (2004), Application of the cross wavelet transform and wavelet coherence to geophysical time series, *Nonlinear Proc. in Geophys., 11*,561-566

Jakowski, N., B. Fichtelmann, A. Jungstand, (1991), Solar activity control of ionospheric and thermospheric processes, *J. Atmos and Terrel Phys., 53*, 1125–1130

Kane, K. P., (1992), Solar cycle variation of foF2, *J. Atmos. Terr. Phys., 54*, 1201

Kelly, M., D. Kotsikopoulos, T. Beach, and D. L. Hysell, (1996), Simultaneous global positioning system and radar observations of equatorial spread F at Kwajalein, *J. Geophys. Res., 101,* 2333

Kugiumtzis, D., (1999), Surrogate data test for nonlinearity including nonmonotonic transforms, *Phys. Rev.* E, *62*, 25

Kutiev, I., S. Watanabe, Y. Otsuka, and A. Saito, (2005), Total electron content behavior over Japan during geomagnetic storms, *J. Geophys. Res. 110(A01308),* doi: 10.1029/2004JA010586

Lastovicka, J., P. Krizan, P. Sauli, and D. Novotna, (2003), Persistence of the planetary wave type oscillations in foF2 over Europe, *Ann. Geophys., 21,* 1543–1552

Liu, J. Y., Y. I. Chen, J. S. Lin, (2003), Statistical investigation of the saturation effects in the ionospheric foF2 versus sunspot, solar radio noise, and solar EUV radiation, *J. Geophys. Res.*, *108*(A2), 1067

Lunt, N., L. Kersley, G. L. Bishop, and A. J. Mazzella Jr., (1999a), The contribution of the protonosphere to GPS total electron content: Experimental measurements, *Radio Sci., 34,* 1273

Lunt, N., L. Kersley, G. L. Bishop, and A. J. Mazzella Jr., G. L. Bailey, (1999b), The protonospheric contribution to GPS total electron content: Two-station measurements, *Radio Sci., 34*, 1281

Mallat, S., (1989), A theory of multiresolution signal decomposition: The wavelet representation, *IEEE Trans. On Pattern Analysis and Machine Intelligence 11,*647-693

Maple, S. L., (1987), *Digital spectral analysis*, Prentice-Hall, New Jersey

Mayaud, P. N., (1980), Derivation, meaning and use of geomagnetic indices, *Geophysical Monograph, 22*

McClintock, W. E., C. A. Barth, R. E. Steele, G. M. Lawrence, and J. G. Timothy, (1982), Rocket-borne instrument with a high-resolution microchannel plate detector for planetary UV spectroscopy, *Appl. Opt., 21*, 3071

McNamara, L. F. and D. H. Smith, (1982), Total electron content of the ionosphere at 30 S, 1967-1974, *J. Atmos. Terr. Phys., 44*, 227.

Mendenhall, W., D. D. Wackerly and D. L. Scheaffer, (1990), *Mathematical statistics with applications*, 4th edition, Duxbury, Belmont

Mendillo, M., H. Risbeth, R. G. Roble, and J. Wroten, (2002), Modelling F2-layer seasonal trends and day-to-day variability driven by coupling with the lower atmosphere, *J. Atmos. Sol. Terr. Phys*., *64,* 1911 –1931

Morlet, J., G. Arens, I. Fourgeau, and D. Giard, (1982), Wave propagation and sampling theory, *Geophysics 47*,203-236

Mursula, K., and B. Zieger, (1996), The 13.5 day periodicity in the Sun, solar wind, and geomagnetic activity: The last three solar cycles, *J. Geophys. Res., 101*, 27,077–27,090

Oppenheim, A. V. and R. W. Schafer, (1989), *Discrete-Time Signal Processing*, Prentice-Hall, New Jersey

Orfanidis, S., (1996), *Introduction to Signal Processing*, Prentice Hall, New Jersey

Pancheva, D.V. and N. J. Mitchell, (2004), Planetary waves and variability of the semidiurnal tide in the mesosphere and lower thermosphere over Esrange (68N, 21E) during winter, *J. Geophys. Res., 109* (A08307), doi: 10.1029

Pancheva, D. and P. Mukhtarov, (2000), Wavelet analysis on transient behavior of tidal amplitude fluctuations observed by meteor radar in the lower thermosphere above Bulgaria, *Ann. Geophys., 18,* 36-331

Pi, X., A. J. Mannucci, U.J. Lindqwister and C. M. Ho, (1997), Monitoring of global ionospheric irregularities using a worldwide GPS network, *Geophys. Res. Lett., 24*, 2283

Powell, F. R., P. W. Vedder, J. F. Lindblom, and S. F. Powell (1990), Thin film filter performance for extreme ultraviolet and X-ray applications, *Opt. Eng., 26*, 614.

Proakis, J. G. and D. G. Manolakis, (1996), *Digital signal processing: principle, algorithm and applications,* Prentice Hall, New Jersey

Prolss, G. W., (1995), *Ionospheric F-region storms.* In Handbook of atmospheric electrodynamics, 2, CRC press, Boca Raton, 195-248

Reinisch, B. W. and X. Huang, (1983), Automatic calculation of electron density profiles from digital Ionograms, 3, processing of bottomside Ionograms, *Radio Sci., 18,* 477

Reinisch, B. W., (1996), Modern Ionosondes, in *Modern Ionospheric Science*, edited by H. Kohl, R. Ruster, and K. Schlegel, European Geophysical Society, 37191, Katlenburg-Lindau, Germany, 440-458

Richards, P. G., D.G. Torr, M.J Buonsanto, D.P. Sipler, (1994), Ionospheric effects of the March 1990 magnetic storm: Comparison of theory and measurement, *J. Geophys. Res., 99 (A12),* 23359-23365

Richards, P, G., (2002), Ion and neutral density variations during ionospheric storms in September 1974: Comparison of measurement and models, *J. Geophys. Res.*, *107*(A11), 1361, doi:10.1029/2002JA009278

Richards, P. G., D.G. Torr, B.W.Reinish, and R.R. Gamache, R.R., (1994), F2 peak electron density at Millstone Hill and Hobart: Comparison of theory and measurement at solar maximum, *J. Geophys. Res.*, *99*(A8) 15,005-15,016

Rishbeth, H., (1991), F-region and thermospheric dynamics, *J. Geomag. Geoelectr., 43,* 513-524

Rishbeth, H., (1993), Day-to-day ionospheric variations in a period of high solar activity, *J. Atmos. Terr. Phys., 55,* 165

Rishbeth, H., (2001), The centenary of solar-terrestrial physics, *J. Atmos. Sol. Terr. Phys., 63,* 1883-1890

Rishbeth, H.,M. Mendillo, (2001), Patterns of F2-layer variability, *J. Atmos. Sol. Terr. Phys*., *63*, 1661–1680

Rosenblatt, M., (1985), *Stationary sequences and random fields*, Birkhauser, Boston

Schrijver, C. J, C. Zwaan, (2000), *Solar and stellar magnetic activity,* Cambridge, Mass.

Smith, M. J. S. and T. P. Barnwell III, (1986), Exact reconstruction from tree-structured subband coders, *IEEE Trans. on Acoustics, Speech and Signal processing 34,* 431-441

Smith, M. J. S. and T. P. Barnwell III, (1987), A new filter bank theory for time-frequency representations, *IEEE Trans. on Acoustics, Speech and Signal processing 35,* 314-327

Solomon, S. C., S. M. Bailey, T. N. Woods, (2001), Effect of solar soft X-rays on the lower ionosphere, *Geophys. Res. Lett., 28,* 11, 2149-2152

Strang, G. and T. Q Nguyen, (1996), *Wavelets and filter banks,* Wellesley-Cambridge press, Wellesley, Massachusetts

Su, Y. Z, G. J. Bailey, S. Fukao, (1999), Altitude dependences in the solar activity variations of the ionospheric electron density, *J. Geophys. Res.*, *104*(A7), 14879-14891

Thomason, N. R., C. J. Rodger, R. L. Dowdon, (2004), Ionosphere gives size to greatest solar flares, *Geophys. Res. Lett., 31,* L068063

Tsurutani, B. T, D. L. Judge, P. L. Guarnieri, A. R. Jones, J. Nuttall, G. A. Zambon, L. Didkovsky, (2005), The October 28, 2003 extreme EUV solar flare and resultant extreme ionospheric effects: Comparison to other Halloween events and the Bastille Day event, *Geophys. Res. Lett., 32,* L03S09

Vaidyanathan, P. P, (1987), Theory and design of M-channel maximally decimated quadrature mirror filters with arbitrary M, having the perfect reconstruction property., *IEEE Trans. on Acoustics, Speech and Signal processing 35,* 476-492

Vaidyanathan, P. P, (1993), *Miltirate Systems and Filter banks,* Prentice-Hall, Englewood-Cliffs, New Jersey

Valladares C. E., S. Basu, K. Groves, M.P. Hagan, D. Hysell, A. Mazzella, R. Sheehan, (2001), Measurements of equatorial spread-F ionospheric conditions using a latitudinal chain of GPS receivers, *J. Geophys. Res.*, *106,* 29133

Vetterli, M., (1986), Filter banks allowing for perfect reconstruction, *Signal processing 10*, 219-244

Wang, X., R. Eastes, S. Weichecki Vergara, S. Bailey, C. Valladares, T. Woods, (2006), On the short-term relationship between solar soft X-ray irradiances and equatorial Total Electron Content (TEC), *J. Geophys. Res.*, *111(*A10S15), doi:10.1029

Wang, X., R. Eastes, B. Reinisch, S. Bailey, C. Valladares, T. Woods, (2007), Short-term relationship between solar irradiances and equatorial peak electron densities, *J. Geophys. Res.* (In press)

Welch, P.D., (1967), The Use of Fast Fourier Transform for the Estimation of Power Spectra: A Method Based on Time Averaging Over Short, Modified Periodograms, *IEEE Trans. Audio Electroacoustics, AU-15,* (June 1967), 70-73

Woods, T., F. Eparvier, S. Bailey, S. C. Solomon, G. Rottman, G. Lawrence, R. Roble, O. R. White, J. Lean, and W. K. Tobiska (1998), TIMED Solar EUV Experiment, *SPIE Proc.,* 3442, 180

Woods, T., E. Rodgers, S. Bailey, F. Eparvier, and G. Ucker (1999a), TIMED Solar EUV Experiment: Pre-flight calibration results for the XUV Photometer System, *SPIE Proc.,* 3756, 255

Zhang, D. H., Z. Xiao, K. Igarashi, G.Y. Ma, (2002), GPS-derived ionospheric total electron content response to a solar flare that occurred on 14 July 2000, *Radio Sci.,* *37*(5), 1086, doi:10.1029/2001RS002542